



1 **Vertical wind retrieved by airborne lidar and analysis of**
2 **island induced gravity waves in combination with**
3 **numerical models and in-situ particle measurements**

4
5 **F. Chouza¹, O. Reitebuch¹, M. Jähn², S. Rahm¹, B. Weinzierl^{1,3}**

6 [1]{Deutsches Zentrum für Luft- und Raumfahrt (DLR), Institut für Physik der Atmosphäre,
7 Oberpfaffenhofen, Germany}

8 [2]{Leibniz Institute for Tropospheric Research, Leipzig, Germany}

9 [3]{Ludwig-Maximilians-Universität München (LMU), Meteorologisches Institut, München,
10 Germany}

11 Correspondence to: F. Chouza (fernando.chouza@dlr.de)

12

13 **Abstract**

14 This study presents the analysis of island induced gravity waves observed by an airborne
15 Doppler wind lidar (DWL) during SALTRACE. First, the instrumental corrections required
16 for the retrieval of high spatial resolution vertical wind measurements from an airborne DWL
17 are presented and the measurement accuracy estimated by means of two different methods.
18 The estimated systematic error is below -0.05 m s^{-1} for the selected case of study, while the
19 random error lies between 0.1 m s^{-1} and 0.16 m s^{-1} depending on the estimation method.

20 Then, the presented method is applied to two measurement flights during which the presence
21 of island induced gravity waves was detected. The first case corresponds to a research flight
22 conducted on 17 June 2013 in the Cape Verde islands region, while the second case
23 corresponds to a measurement flight on 26 June 2013 in the Barbados region. The presence of
24 trapped lee waves predicted by the calculated Scorer parameter profiles was confirmed by the
25 lidar and in-situ observations. The DWL measurements are used in combination with in-situ
26 wind and particle number density measurements, large eddy simulations (LES), and wavelet
27 analysis to determine the main characteristics of the observed island induced trapped waves.

28



1 **1 Introduction**

2 Large amounts of Saharan dust are transported every year across the Atlantic into the
3 Caribbean region (e.g. Prospero, 1999; Prospero et al., 2013). The Cape Verde and Barbados
4 islands, located along the main Saharan dust transport path, interact with the dust advective
5 flow through different mechanisms, including island induced gravity waves. This interaction
6 can give place to changes in the dust sedimentation rates, the vertical mixing, and clouds
7 formation among other effects (e.g. Engelmann et al., 2011; Savijärvi and Matthews, 2004;
8 Cui et al., 2012).

9 In order to provide new insights into the different processes that affect the Saharan mineral
10 dust during the long-range transport from the Sahara into the Caribbean, the Saharan Aerosol
11 Long-range Transport and Aerosol-Cloud-Interaction Experiment (SALTRACE:
12 <http://www.pa.op.dlr.de/saltrace>) took place in June/July 2013. In the framework of
13 SALTRACE, 31 research flights were conducted between 10 June and 15 July 2013 by the
14 DLR (Deutsches Zentrum für Luft- und Raumfahrt) research aircraft Falcon, including several
15 flights in the Cape Verde islands region and Barbados. The payload deployed on board the
16 Falcon included a DWL (Doppler Wind lidar), aerosol, temperature, humidity and wind speed
17 in-situ sensors, and dropsondes. The measurement data set generated during the SALTRACE
18 campaign provides a good opportunity to study the generation of gravity waves by the Cape
19 Verde islands and Barbados and their interaction with the Saharan dust during its transport.

20 Although it is well known that gravity waves can be generated by orography (Smith, 1980;
21 Alexander and Grimsdell, 2013) and thermal effects (e.g. Baik, 1992; Savijärvi and
22 Matthews, 2004), the relative impact of these two mechanisms depend on the specific island
23 topography, location and atmospheric conditions. Previous large eddy simulation (LES)
24 studies performed in the Cape Verde region (Engelmann et al., 2011), conducted during the
25 SAMUM-2 campaign, showed that a flat island with the characteristics of the Santiago Island
26 (Cape Verde) can induce the generation of gravity waves and enhance the aerosol downward
27 mixing, only through its heat island effect, without taking into account its orography. Another
28 recent LES study (Jähn et al., 2015b) conducted in the Barbados area also revealed the
29 presence of island induced gravity waves on the lee side of the island and provided further
30 insight into the dust turbulent downward mixing, cloud generation and boundary layer
31 modification in the lee side of the island. In contrast with the previous case, the heating effect
32 and the orography were taken into account in this case.



1 Although several different measurement techniques were used to analyse gravity waves (e.g.
2 Kirkwood, et al., 2010; Kühnlein et al., 2013; Ehard et al., 2015), including, but not limited
3 to, ground based lidars and radars, airborne lidars and in-situ sensors, balloons and satellites,
4 the use of airborne Doppler wind lidars is unusual (Bluman and Hart, 1988). While horizontal
5 wind measurements retrieved by airborne DWLs are frequently found in the literature
6 (Reitebuch et al., 2001; Reitebuch et al., 2003; Weissmann et al., 2005; De Wekker et al.,
7 2012; Kavaya et al., 2014), only a few high resolution measurements of vertical winds are
8 reported (Kiemle et al., 2007; Kiemle et al., 2011; Emmitt and Godwin, 2014). Usually, DWLs
9 provide measurements of the relative wind speed between the instrument and the sensed
10 atmospheric volume every second. Using a conically arranged measurement pattern and the
11 velocity-azimuth display (VAD) technique (Reitebuch et al., 2001), three dimensional
12 measurements of the wind field can be retrieved based on a few tens of measurements, which
13 corresponds to a spatial resolution on the order of a few kilometres for airborne platforms.
14 Although this is enough to resolve the main features of the horizontal wind field, a higher
15 spatial resolution in the vertical wind component is required to perform turbulence, eddy flux
16 and short-wavelength gravity wave studies.

17 In order to increase the spatial resolution of the vertical wind retrieval, fixed downward
18 (nadir) pointing measurements can be performed instead of the previously mentioned conical
19 scanning pattern. This allows the retrieval of one measurement every second, which is
20 equivalent to a spatial resolution of around 50 m to 200 m, depending on the aircraft type and
21 speed. Nevertheless, there are some problems associated with this technique which have to be
22 addressed to allow an accurate vertical wind retrieval.

23 The paper is organized as follows. Section 2 provides a brief description of the coherent DWL
24 mounted on the Falcon research aircraft of DLR during SALTRACE and an overview of the
25 method applied to retrieve high spatial resolution vertical wind measurements. Then, in
26 Section 3, the resulting data set is used in combination with in-situ observations and large
27 eddy simulations to analyse the generation, evolution and interaction with aerosols of island
28 induced gravity waves. Two different cases were analysed: one in the Cape Verde region and
29 the other in the Barbados Island. The measurements corresponding to both cases and
30 simulation results from the second case are compared in order to determine the similarities
31 and differences between the two cases, as well as the ability of the simulation to reproduce the



1 observed waves and provide a context to the in-situ and lidar measurements. Finally, Section
2 4 provides a summary and concluding remarks.

3

4 **2 Coherent DWL instrument**

5 **2.1 Instrument description**

6 During SALTRACE an airborne coherent DWL was deployed on board the DLR Falcon 20
7 research aircraft. The system, based on an instrument developed by CLR Photonics
8 (Henderson et al., 1993), today Lockheed Martin Coherent Technologies (LMCT), was
9 modified by DLR (Köpp et al., 2004) to provide airborne measurement capabilities. The
10 transceiver head, holding the diode pumped solid-state Tm:LuAG laser, the 10.8 cm diameter
11 afocal transceiver telescope, the receiver optics and detectors, and a double wedge scanner is
12 mounted on the front part of the passenger cabin (Fig. 1), while the laser power supply, the
13 cooling unit, the data acquisition and control electronics are mounted in two separated racks.

14 The lidar operates at a wavelength of 2.02254 μm , with a pulse full width at half maximum
15 (FWHM) of 400 ns, a pulse energy of 1-2 mJ, and a repetition frequency of 500 Hz. The key
16 system specifications are presented in Table 1.

17 Based on the heterodyne technique, DWLs are able to measure the projection of the relative
18 velocity between the lidar and wind along the laser pulse propagation direction. The
19 backscattered atmospheric signal frequency, which was affected by the Doppler effect, is
20 measured by mixing the backscatter signal with the laser source used to seed the outgoing
21 sensing pulse. Because the outgoing pulse is frequency shifted by 100 MHz with respect to
22 the seeding laser by an acousto-optical modulator (AOM), the DWL is able to resolve the
23 magnitude and sign of the Doppler induced frequency shift. Finally, applying the Doppler
24 equation, the measured frequency difference can be converted to a relative speed.

25 As mentioned before, the DWL has a dual wedge scanner system mounted in front of the
26 transceiver telescope. While single wedge scanners allow fixed line of sight (LOS) and
27 conical scan patterns with a fixed off-nadir angle, dual wedge scanning systems allow the
28 generation of arbitrary scanning patterns (Rahm et al., 2007; Käsler et al., 2010). In the case
29 of the DLR DWL, the dual wedge scanner system consists of two independently rotating
30 silicon wedges, with a wedge angle of 6° and their flat sides parallel arranged. Based on the



1 vector form of the Snell's law and the angular measurements θ_1 and θ_2 provided by the rotary
2 encoders attached to each wedge, the DWL pointing direction $\vec{L}_{DWL}(\theta_1, \theta_2)$ can be calculated
3 (Amirault et al., 1985).

4 Particularly in the case of airborne measurements, two operation modes are used: the conical
5 step and stare and the nadir pointing mode. The step and stare mode, retrieve horizontal wind
6 speed and direction based on the previously mentioned VAD technique (Reitebuch, 2012;
7 Weissmann et al., 2005; Reitebuch et al., 2001). The measurement pattern consists of a set of
8 up to 24 regularly spaced pointing directions \vec{L}_{DWL} distributed in a conical geometry with an
9 accumulation time of 1 s or 2 s for each position. On the other side, for the retrieval of vertical
10 wind speed, the LOS vector \vec{L}_{DWL} is set pointing approximately in nadir direction, and the
11 measurements are performed with an accumulation time of 1 s.

12 While horizontal wind speeds are about one order of magnitude lower than the aircraft speed
13 (approx. 180 m s^{-1}), vertical winds are usually two orders of magnitude lower. Because the
14 DWLs measure relative speed between the instrument and the sensed atmospheric volume,
15 especially accurate measurements of the aircraft speed, orientation, and DWL relative position
16 with respect to the aircraft have to be achieved in order to subtract the aircraft speed
17 component from the DWL measurement. A second problem associated with this measurement
18 scheme is the projection of the horizontal wind speed. A deviation of the DWL LOS from the
19 nadir direction introduces a projection of the horizontal wind speed in the vertical wind
20 measurement that can be only partially corrected.

21 Although the vertical wind retrieval would require a constant nadir pointing LOS in order to
22 avoid the projection of the horizontal wind speed, the system configuration during
23 SALTRACE did not perform an automatic correction of the LOS. However, a manual
24 adjustment of the LOS was performed during flight to partially correct the pitch angle of the
25 aircraft. The \vec{L}_{DWL} vector was set with an offset angle between -2° and -2.5° around the Y axis
26 to partially compensate, in combination with the DWL mounting angle, the aircraft pitch
27 (normally between 4° and 6°).

28 **2.2 Calculation of the LOS pointing direction**

29 Based on the angles read by the scanner encoders, the output beam direction with respect to
30 the DWL frame can be determined. Nevertheless, because the system is mounted on an



1 aircraft which changes its orientation during the flight, additional transformations are required
 2 to relate the lidar LOS vector to an Earth-fixed reference frame.

3 As can be seen in Fig. 1, the DWL transceiver head is mounted on the front part of the DLR
 4 Falcon 20 research aircraft, with the transceiver telescope pointing downwards to allow the
 5 measurement of vertical profiles. The orientation of the transceiver head with respect to the
 6 aircraft frame (IRS frame) can be described by a set of Euler angles
 7 $\vec{\theta}_{\text{DWL}} = [r_{\text{DWL}}, p_{\text{DWL}}, y_{\text{DWL}}]$ which are determined by the mechanical mounting of the lidar,
 8 where r is the roll angle, p the pitch angle and y the yaw angle. Although the magnitude of
 9 these angles is small (on the order of a few degrees), they have to be taken into account to
 10 avoid large systematic errors in the wind retrieval algorithm. A second set of Euler angles
 11 $\vec{\theta}_{\text{IRS}} = [r_{\text{IRS}}, p_{\text{IRS}}, y_{\text{IRS}}]$, measured by the IRS of the aircraft, describe the orientation of the
 12 aircraft with respect to a local NED (North-East-Down) Earth reference frame.

13 The LOS vector \vec{L}_{DWL} calculated based on the angles measured by the scanner encoders can
 14 be translated to a reference frame fixed to the Earth applying the following equation

$$15 \quad \vec{L} = \begin{bmatrix} L_N \\ L_E \\ L_D \end{bmatrix} = C_{\text{NED}}^{\text{IRS}}(\vec{\theta}_{\text{IRS}}) \cdot C_{\text{IRS}}^{\text{DWL}}(\vec{\theta}_{\text{DWL}}) \cdot \vec{L}_{\text{DWL}}(\theta_1, \theta_2) \quad (1)$$

16 where \vec{L} is the LOS vector \vec{L}_{DWL} referred to the Earth reference system for a given aircraft
 17 orientation $\vec{\theta}_{\text{IRS}}$, $C_{\text{NED}}^{\text{IRS}}(\vec{\theta}_{\text{IRS}})$ is a coordinate transformation matrix between the IRS and the
 18 NED reference frames based on the IRS measurements and the $C_{\text{IRS}}^{\text{DWL}}(\vec{\theta}_{\text{DWL}})$ is a coordinate
 19 transformation matrix between the DWL reference frame and IRS reference frame, calculated
 20 for a set of mounting angles $\vec{\theta}_{\text{DWL}}$ (Grewal et al., 2007).

21 2.3 Vertical wind retrieval method

22 For an airborne DWL with a given pointing direction, the retrieved velocity corresponds to
 23 the relative speed, projected on the laser beam direction of propagation, between the aircraft
 24 and the atmospheric target or ground surface contained by the sensed volume at distance R .
 25 This relation is summarized by the equation

$$26 \quad v_{\text{DWL}}(R) = \vec{L} \cdot \vec{v}_{\text{ac}} + \vec{L} \cdot \vec{V}(R) + \vec{L} \cdot \vec{w}(R) \quad (2)$$



1 Where $v_{\text{DWL}}(R)$ is the speed measured by the airborne DWL, \vec{L} is the beam direction of
 2 propagation or LOS, \vec{v}_{ac} is the aircraft speed, $\vec{V}(R) = [u(R), v(R), 0]$ and $\vec{w}(R) =$
 3 $[0, 0, w(R)]$ are the horizontal and the vertical component of the wind speed respectively. In
 4 all cases, the vectors are referred to an Earth reference frame.

5 The first step in the wind retrieval process is the removal of the aircraft speed projection on
 6 the measured LOS. While accurate measurements of the aircraft speed are obtained from a
 7 GPS system mounted on the aircraft, the LOS vector \vec{L} is determined based on the angle
 8 measurements of the scanner encoders, the transceiver mounting orientation and the aircraft
 9 orientation measured by the IRS.

10 As mentioned in the previous section, the exact transceiver head mounting angles can be
 11 derived from DWL measurements. The proposed method for the mounting angles $\vec{\theta}_{\text{DWL}}$
 12 estimation is based on surface returns. Previous studies used the fact that the land is immobile
 13 to derive alignment parameters for airborne Doppler radars (Bosart et al., 2002) and lidars
 14 (Reitebuch et al., 2001; Kavaya et al., 2014). Although this assumption is valid for the case of
 15 land returns, in the case of sea surface returns (which is the case of most surface retrievals
 16 during SALTRACE), the wind induced movement of the surface can introduce non
 17 depreciable offsets in the retrievals. On the other side, deviations perpendicular to the flight
 18 direction are hard to resolve using only surface speed measurements because this parameter is
 19 less sensitive to rotations around the aircraft longitudinal axis (roll angle). The proposed
 20 method for the mounting orientation estimation is based on a combination of relative surface
 21 speeds and distances.

22 For the case of a range gate corresponding to land surface return, Eq. (2) is reduced to the
 23 following expression

$$24 \quad v_{\text{DWL}}(R_g) = \vec{L} \cdot \vec{v}_{\text{ac}} \quad (3)$$

25 As was mentioned in the previous section, the DWL mounting angles are small. Based on this
 26 fact, a small angle approximation can be applied to the rotation matrix $C_{\text{IRS}}^{\text{DWL}}$ from Eq. (1),
 27 resulting in the following matrix

$$28 \quad C_{\text{IRS}}^{\text{DWL}}(\vec{\theta}_{\text{DWL}}) \approx \begin{pmatrix} 1 & -y_{\text{DWL}} & p_{\text{DWL}} \\ y_{\text{DWL}} & 1 & -r_{\text{DWL}} \\ -p_{\text{DWL}} & r_{\text{DWL}} & 1 \end{pmatrix} \quad (4)$$



1 Then, substituting Eq. (4) in Eq. (1) and the result in Eq. (3), we can write the following linear
 2 equation

$$3 \quad v_{\text{DWL}}(R_g) = C_{\text{NED}}^{\text{IRS}}(\vec{\theta}_{\text{IRS}}) \cdot \begin{pmatrix} 1 & -y_{\text{DWL}} & p_{\text{DWL}} \\ y_{\text{DWL}} & 1 & -r_{\text{DWL}} \\ -p_{\text{DWL}} & r_{\text{DWL}} & 1 \end{pmatrix} \cdot \vec{L}_{\text{DWL}}(\theta_1, \theta_2) \cdot \vec{v}_{\text{ac}} \quad (5)$$

4 Using a set of land surface return measurements obtained by the lidar operating in conical
 5 scanning mode, an overdetermined set of linear equations can be defined. Its solution gives us
 6 an estimation of the DWL mounting orientation $\vec{\theta}_{\text{DWL}}$.

7 Although it is possible to estimate the mounting angles based only on land surface speed
 8 measurements, the additional use of surface distance measurements reduces the amount of
 9 required data points and increases the accuracy of the estimation, especially with respect to
 10 rotations of the transceiver head around the aircraft longitudinal axis r_{DWL} .

11 For a range gate corresponding to sea surface return and neglecting Earth curvature effects,
 12 the measured distance by the lidar can be approximated by

$$13 \quad d_{\text{DWL}}(R_g) = \frac{h_{\text{ac}}}{L_D} \quad (6)$$

14 Where $d_{\text{DWL}}(R_g)$ is the distance measured by the lidar, h_{ac} is the altitude of the DWL
 15 measured by the GPS (World Geodetic System 1984 standard, WGS84) and corrected taking
 16 in account the Earth Gravitational Model 1996 (EGM96, [http://earth-
 17 info.nga.mil/GandG/wgs84/gravitymod/egm96/egm96.html](http://earth-info.nga.mil/GandG/wgs84/gravitymod/egm96/egm96.html)), and L_D is the vertical
 18 component of the LOS vector \vec{L} approximated by Eq. (5). While the use of land surface return
 19 is also possible, it requires additional processing and the use of a DEM (Digital Elevation
 20 Model). For the particular case of SALTRACE, for which most of the measurements were
 21 performed over sea, only the sea surface was used as distance reference for the estimation of
 22 the mounting orientation.

23 In order to characterize the stability of the mounting angles of the DWL, three different
 24 analyses were performed. First, an analysis was done based on the observation of the changes
 25 in the mounting angle for different flight conditions. For a given flight, the surface returns
 26 were grouped according to the flight altitude and the mounting angles retrieved using Eq. (5)
 27 and Eq. (6). For altitudes below 5000 m, the mounting angles showed a slight change with
 28 respect to those retrieved for higher altitudes. This effect can be attributed to small aircraft



1 deformations, mounting angle variation due to the lidar flexible mounting system and the
2 consequent change in the orientation of the lidar with respect to the aircraft IRS.

3 Then, a second stability analysis between different flights was performed. For each flight, the
4 surface returns (land and sea) corresponding to flight altitudes higher than 5000 m, with
5 vertical aircraft speeds lower than 0.05 m s^{-1} and performed using scanning operation mode,
6 were used to retrieve the mounting angles. An equation system based on Eq. (6) was defined
7 for the case of points retrieved from land surface, while Eq. (7) was used for the case of sea
8 surface returns. For flights for which more than 50 land and sea surface return measurements
9 were available, the equation system was solved. The results are presented in Table 2,
10 together with the results obtained for the same flights using only one of both return types.

11 As can be seen in Table 2, the estimated mounting pitch angle p_{DWL} does not show a big
12 difference between both methods. This result is expected because both the distance and the
13 ground speed measurements are strongly affected by deviations in the pitch angle. On the
14 other hand, for the case of the roll mounting angle r_{DWL} , the use of only one method gives
15 place to different solutions between methods and flights, while the combination of both
16 methods gives more stable results. The yaw angle y_{DWL} is better resolved by the speed
17 measurements, which is compatible with the expected behaviour. In general, the simultaneous
18 use of both methods gives more stable results between flights.

19 Finally, because the orientation showed to be stable between different flights, the same
20 method was applied using all sea and ground surface returns which fulfill the altitude, vertical
21 velocity and operation mode previously described, independently of the flight. The
22 coincidence with the flight by flight calculation using distance and velocity equations is better
23 than 0.1° for pitch and yaw angles, and better than 0.2° for the roll angle estimation.

24 The mounting orientation estimation resulting from the last calculation with all flights
25 $\vec{\theta}_{\text{DWL}} = [0.98^\circ; -2.08^\circ; 1.62^\circ]$ was used in the horizontal and vertical wind retrieval process
26 for all SALTRACE flights legs flown above 5000 m. For the case of low level flight legs
27 ($<5000 \text{ m}$) during which the aircraft deformation was relevant and surface returns are
28 available, two different approaches can be applied to correct this effect. If the surface
29 measurements were obtained by the lidar operating in scanning mode, it is possible to
30 recalculate the DWL mounting orientation based on those observations. In the other hand, if
31 the measurements were performed in nadir pointing mode, the mean difference between the



1 surface return speed measured by the lidar $v_{\text{DWL}}(R_g)$ and their estimation $\vec{L} \cdot \vec{v}_{\text{ac}}$ can be
2 subtracted from the retrievals corresponding to atmospheric range gates $v_{\text{DWL}}(R)$ in order to
3 partially compensate this effect.

4 For the particular case of vertical wind measurements, the LOS vector \vec{L} has to be pointing
5 downwards during the measurements. The better this condition is fulfilled; the better will be
6 the retrieved vertical wind measurements. Small deviations from vertical pointing, introduces
7 a projection of the horizontal wind speed on the LOS which cannot be distinguished from the
8 vertical wind component. For example, for an horizontal wind speed of 10 m s^{-1} and a
9 direction contrary to the flight direction, a deviation of 0.5° from nadir in the pitch axis will
10 introduce a bias of 0.09 m s^{-1} in the measured LOS speed.

11 As mentioned in Sec. 2.1, because no mounting orientation characterization was performed
12 before the campaign and no automatic LOS correction was implemented to compensate
13 changes in the aircraft orientation; the vertical wind measurements include the effects of the
14 horizontal wind projection on the LOS $\vec{L} \cdot \vec{V}(R)$. To partially correct this effect, estimations
15 of the horizontal wind speed based on DWL measurements, dropsondes and models from the
16 same flight leg or close were used.

17 **2.4 Validation of method and error analysis**

18 In order to test and validate the method presented in the previous section, the measurements
19 corresponding to a flight performed on 20 June 2013 were used. As a first approach, the
20 mounting angles retrieved in the previous section were applied to estimate the surface return
21 speed for the particular case of the leg flown between 10:31 and 10:45 LT at an altitude of
22 2900 m during which the lidar was operating in nadir pointing mode. The resulting surface
23 speed measurements show a standard deviation of $\sim 0.4 \text{ m s}^{-1}$ for sea return points and $\sim 0.1 \text{ m}$
24 s^{-1} for land return points with a systematic difference of around -0.4 m s^{-1} between the
25 expected and the measured ground speed values. This difference, as explained before, can be
26 attributed to a change in the relative position of the lidar and the aircraft IRS due to aircraft
27 deformations during low level flights. For this case, because measurements using scanning
28 mode were performed during the same flight and under similar speed and altitude conditions,
29 new mounting angles were calculated. The major difference of the recalculated values
30 $\vec{\theta}_{\text{DWL}} = [0.96^\circ; -2.24^\circ; 1.68^\circ]$ is in the pitch angle (0.16°), which is consistent with
31 measurements performed to analyze the stability of the mounting orientation during the flight.



1 The recalculated mean difference between the measurements and the estimations obtained
2 based on the new set of mounting angles is 0.036 ms^{-1} , while the standard deviation
3 corresponding to land and sea returns remains the same.

4 From the in-situ vertical wind speed measurements of the Falcon nose boom sensors
5 presented in Fig. 2a, it can be seen that the Falcon was flying through gravity waves. These
6 waves induce a change in the aircraft pitch (Fig. 2a), which in turn induce a change in the
7 LOS of the lidar and, therefore, a varying horizontal wind projection with a contribution
8 between $\pm 0.15 \text{ ms}^{-1}$ for a horizontal speed of 12 ms^{-1} . In order to partially correct this
9 feedback effect, an estimation of the horizontal wind speed and direction obtained from a
10 previous measurement leg (10:00 to 10:15 LT) was used (Fig. 2b). The resulting projection
11 $\vec{L} \cdot \vec{V}(\text{R})$ is shown in Fig. 2c.

12 Finally, the vertical wind speed can be determined subtracting the aircraft speed and
13 horizontal wind speed projections from the relative speed measured by the DWL. The
14 resulting vertical wind speeds are presented in Fig. 3a together with a comparison between the
15 in-situ vertical wind speeds measured by the Falcon (Fig.4). It has to be noted that the closest
16 DWL measurements are around 500 m below the aircraft, which could explain the difference
17 between the amplitude of the DWL and in-situ measurements. Despite this altitude difference,
18 the main features of the vertical wind field (amplitude, oscillation frequency and mean value)
19 are comparable.

20 In order to estimate the DWL measurement error, two methods were applied. The first method
21 (Frehlich, 2001; O'Connor et al., 2010) is based on the frequency spectrum of the retrieved
22 velocity. For the flight leg presented in Fig. 3, the spectra corresponding to the retrieved
23 vertical wind speed from the DWL measurements at altitude of 2300 m were calculated and
24 averaged. A total of 32 spectra of 64 samples were calculated. A 50% window overlap factor,
25 a Hanning window and a zero-padding of the missing values was applied to each window for
26 each spectrum calculation (Kiemle et al., 2011). The resulting spectrum, presented in Fig. 4,
27 shows that for frequencies higher than 0.2 Hz the spectrum corresponding to the DWL tends
28 to a constant value, departing from the Kolmogorov's $-5/3$ law. This high frequency region
29 represents the spectrum of the random measurement noise. The standard deviation of the
30 measurement is then estimated as the mean of the spectra over its constant region. Based on
31 the presented case, the random measurement error was estimated to be $\sigma_e = 0.16 \text{ ms}^{-1}$.



1 The second method, based on ground return analysis, relies on the fact that the ground surface
2 is not moving. For an ideal system, the difference between the ground return speed measured
3 by the lidar and the aircraft speed projected on the beam direction has to be zero. For a real
4 DWL, the mean of this difference corresponds to the systematic measurement error, while its
5 variations correspond to the lidar random error for high SNR. Based on the land returns, the
6 estimated systematic error is $\mu_e = -0.05 \text{ m s}^{-1}$ and random error standard deviation is
7 $\sigma_e = 0.10 \text{ ms}^{-1}$.

8 The errors estimated based on both approaches are on the same order of magnitude. Because
9 the measurement error depends on many different parameters, like SNR, turbulence and flight
10 conditions, relatively small variations in the uncertainty are expected for differing
11 measurement situations.

12 **3 Case studies**

13 The vertical wind retrieval method presented in the previous section was applied to the DWL
14 measurements corresponding to two SALTRACE flights during which gravity waves were
15 observed. While the flight corresponding to the first of case study took place on 17 June 2013
16 in the Cape Verde region (close to the Saharan dust source), the flight analysed in the second
17 case study was conducted in the Barbados region, where the main SALTRACE supersite was
18 located.

19 **3.1 Case 1: Island induced trapped lee waves in Cape Verde (17 June 2013)**

20 The synoptic conditions, derived from the ECMWF Era-Interim reanalysis, on the Cape
21 Verde islands at 12:00 UTC (11:00 LT) on 17 June 2013 are show for 1000 hPa and 700 hPa
22 pressure levels in Fig. 5 (upper panels). Northerly trade winds with a speed on the order of 5-
23 10 m s^{-1} are visible at the lower pressure level. For the upper pressure level the wind changes
24 to easterly direction, which is compatible with the presence of the African Easterly Jet (AEJ).

25 During the morning of 17 June 2013, the Falcon performed a measurement flight in the Cape
26 Verde islands region, departing from Sal and landing on Praia (Fig. S1). The flight consisted
27 of three legs between Sal and Praia islands, at altitudes of 4100 m, 2500 m and 900 m
28 respectively. During the ascent phase of the flight, the in-situ sensors on board the aircraft
29 recorded vertical profiles of potential temperature, wind speed and direction (Fig 6a). The
30 horizontal winds retrieved by the DWL during segments of the 1st and 2nd leg (not shown)
31 indicate that the values retrieved by the in-situ sensors are representative of the whole flight



1 area and time period. For altitudes below 500 m, a neutrally stratified layer with northerly
2 trade winds can be observed. This layer is capped by a thick strongly stratified trade inversion
3 layer (between 500 m and 2000 m) on which the wind direction exhibits a strong shear and a
4 change to north-easterly direction. Above this inversion, the atmosphere shows a weak
5 stratification and relatively constant wind speed and direction. These observations are
6 compatible with the synoptic situation previously described. Based on the in-situ
7 measurements, a profile of the Scorer parameter was calculated (Fig 6b).

8 According to linear mountain wave theory (e.g. Durran, 1990), the waves that can propagate
9 vertically in the atmosphere can be derived by the use of the Scorer parameter l^2 (Scorer,
10 1949), given by:

$$11 \quad l^2 = \frac{N^2}{U^2} - \frac{1}{U} \frac{d^2 U}{dz^2} \quad (7)$$

12 where N is the Brunt-Väisälä frequency and U is the cross-mountain wind speed. Since the
13 difficulty to estimate the second derivate of the wind from real data, an approximated form of
14 the Scorer parameter which neglects the second term (shear term) is used in this study. This
15 simplification is allowed due to the fact that the shear term is dominated by oscillations with
16 wavelengths much smaller than for the waves under analysis (Smith et al., 2002). An
17 additional validation of this approximation was performed based on temperature, humidity
18 and wind speed vertical profiles retrieved from the ECMWF ERA-Interim reanalysis
19 presented in Fig. 5. The Scorer parameter profile calculated based on the model output and
20 including the shear term (not shown) exhibited a similar structure to the approximated profile
21 calculated from the Falcon in-situ measurements.

22 According to the theory, a wave with wavelength λ and an associated wave number $k = \frac{2\pi}{\lambda}$
23 can propagate in the atmosphere if $k^2 < l^2$; otherwise, the wave is evanescent. Trapped lee
24 waves are expected when a layer with high Scorer parameter is bounded by layers with low
25 Scorer parameter. Under such conditions, the energy of the gravity waves is mainly confined
26 in the layer with high Scorer parameter (Durran et al., 2015). As can be seen in Fig. 6b, the
27 conditions for the development of trapped waves are fulfilled for altitudes between 500 m and
28 2000 m, which are coincident with the trade inversion layer lower and upper bound.

29 Another important parameter to take in account for the study of lee waves is the inverse
30 Froude number, defined as:



$$1 \quad F = \frac{Nh}{U} \quad (8)$$

2 where N is the Brunt-Väisälä frequency, h is the island height and U is the cross-mountain
3 wind speed. For an inverse Froude number between 0 and 0.5, the flow behaves as described
4 by the linear theory and waves are expected to form in the lee side of the island (Baines and
5 Hoinka, 1985). For this case study, the Brunt-Väisälä frequency associated with the boundary
6 layer (below 500m) is approximately $N = 0.01 \text{ s}^{-1}$. This situation leads, together with an
7 inflow speed of 10 m s^{-1} and a maximum island height of 380 m, to a linear flow condition
8 ($F = 0.38$).

9 The DWL vertical wind measurements presented in Fig. 7a confirm the existence of trapped
10 waves between 500 m and 1500 m. At first glance, an apparent wavelength of approximately
11 5 km and a maximum peak-to-peak amplitude of 1.5 m s^{-1} can be estimated from the
12 measurements presented in Fig. 7a. Unfortunately, although the legs were flown at different
13 altitudes, all were performed along the same track. For this reason, only the apparent
14 wavelength can be estimated from these measurements. This apparent wavelength is always
15 larger than the actual one and related to the angle defined between the flight track and the
16 propagation direction of the waves. Based on the apparent wavelength, the associated
17 apparent wave number was calculated and plotted together with the Scorer parameter profile
18 (Fig. 6b). It can be seen that for the layer on which the trapped waves are observed, the Scorer
19 condition for wave propagation $k^2 < l^2$ is fulfilled, while, for altitudes above 1500 m where
20 evanescent waves are expected ($k^2 > l^2$), the waves exhibit a strong reduction in their
21 amplitude as a function of the altitude (0.6 m s^{-1} at 2100 m and 0.4 m s^{-1} at 2600 m, Fig. 7c).

22 Together with the DWL vertical winds, a set of vertical wind speed measurements was
23 retrieved by the Falcon in-situ sensors along each measurement leg (Figs. 7b, c and d).
24 Although the vertical wind measurements from the DWL provide a better image of the
25 vertical extension of the wave ducting, the evanescent propagation regime, and the amplitude
26 of the waves than the in-situ measurements, the DWL measurements of this case study covers
27 only half of the 1st and one third of the 2nd leg, limiting the spectral range that can be analysed
28 from those measurements. In order to complement the DWL measurements and obtain a more
29 precise picture of the spectral components and extension of the observed waves, the wavelet
30 transform technique using a Morlet wavelet (6th order) was applied (Torrence and Compo,
31 1998; Woods and Smith, 2010) to the in-situ vertical wind measurements of the three
32 measurement legs. Unlike the Fourier transformation, which can only retrieve the frequency



1 of the signal, the wavelet analysis is able to temporally resolve the frequencies of a given
2 signal, similar to the short-time Fourier transformation. For this reason and because the
3 measured waves are restricted to a fraction of the measurement period the wavelet analysis is
4 more adequate than a simple Fourier transformation. The in-situ measurements, acquired with
5 a temporal resolution of 1 Hz, were linearly interpolated to a regular spatial grid of 200 m
6 resolution before applying the wavelet transformation to the acquired datasets.

7 Figure 8 shows the calculated spectral components corresponding to the three legs in-situ
8 vertical wind measurements. While the lower leg (Fig. 8, lower panel) exhibits one dominant
9 spectral component with an associated apparent wavelength of 5.2 km, the 2nd leg (Fig. 8, mid
10 panel) shows two spectral peaks with apparent wavelengths of 4.5 km and 15.7 km, and the
11 3rd leg (Fig. 8, upper panel) three peaks with apparent wavelengths of 4.5 km, 7.53 km and
12 16.5 km. Although some variability in the wavelengths is observed between legs, the modes
13 seem to be in even-harmonic relation. The shorter mode, present in all three legs, shows a
14 strong attenuation in the upper two legs, compatible with the evanescent propagation regime.
15 In contrast, the longer mode, present in the upper two legs, is only slightly attenuated.
16 Previous studies on trapped lee waves (Georgelin and Lott, 2001) showed the presence of
17 upward propagating leaked harmonics above the wave duct. In contrast to that case, the
18 spectral analysis of the lower leg doesn't show the presence of the harmonics observed in the
19 upper two, which can be attributed to different reasons. On one side, the longer modes have
20 wavelengths comparable to the length of the measurements leg, which limits the confidence
21 of this observation. This limitation is represented by the cone of influence of the wavelet
22 transform, which indicates the region of the wavelet spectra in which edge effects become
23 relevant. On the other side, although the measurement legs were flown within a short time
24 period, changes in the atmospheric conditions could have introduced a modification in the
25 wave propagation and generation conditions. Finally, taking into account that the
26 measurement legs extend along the downwind region of the Boa Vista and Sal islands, an
27 interaction between waves generated by these two islands cannot be discarded.

28 A second point to be noted from the vertical wind in-situ measurements is the change in the
29 position of the wave crests and troughs between the measurements of the 2nd and 3rd leg,
30 which suggest that the waves are not completely stationary.

31 Together with the vertical wind speed, the DWL measured the backscattered power. Range
32 corrected backscattered power is shown in Fig. 9a together with in-situ vertical winds and



1 Condensation particle counter (CPC) measurements (Weinzierl et al., 2011) for the three legs
2 (Fig. 9b, c, d). The CPC measurements correspond to the number concentration of particles
3 with diameter larger than 14 nm. Figure 9a gives a qualitative picture of the aerosol
4 distribution. Below 500 m, a region of high backscatter corresponding to the marine boundary
5 layer can be recognized. The presence of some clouds on top of the marine boundary layer is
6 indicated by high backscatter regions. The interaction between the trapped waves, a thin
7 aerosol layer which extends between 900 m and 1300 m, and the bottom of the Saharan Air
8 Layer (SAL) can also be noted. The CPC measurements of the 1st and 2nd legs, corresponding
9 to the legs flown in the SAL, show a relatively homogeneous particle number concentration
10 along the leg, with slightly higher values in the upper one.

11 As the 3rd measurement leg was flown at an altitude (1000 m) coincident with a strong
12 gradient in the aerosol concentration (Fig. 9a), the CPC measurements show also the effect of
13 the waves in the aerosol distribution. This explains why the waves are only visible in the third
14 leg and not in the upper two, where the aerosol concentration gradient is close to zero. The
15 phase difference of 90 degrees between the aerosol concentration change and the vertical
16 wind velocity leads to a no net flux condition, where the dust loaded air parcels periodically
17 rise and sink without leading to a net downward or upward dust transport.

18

19 **3.2 Case 2: Island induced trapped lee waves in Barbados (26 June 2013)**

20 **3.2.1 Measurements**

21 During SALTRACE several flights were conducted in the Barbados region. In this study, the
22 measurements corresponding to the flight during the evening of the 26 June 2013 are used to
23 study the presence of island induced gravity waves in the lee side of Barbados (Fig. S2). In
24 this case, the flight path had a cross shape centred in Bridgetown city with constant longitude
25 (1st Leg) and latitude (2nd, 3rd and 4th Legs) at an altitude of approximately 7600 m for the first
26 two legs and 3500 m and 1200 m for the 3rd and 4th legs respectively.

27 The synoptic situation at 00:00 UTC (20:00 LT) on the 27 June 2013 is show in Fig. 5 (lower
28 panels) for 1000 hPa and 700 hPa pressure levels. Easterly winds with a speed of
29 approximately 10 m s⁻¹ can be seen at both pressure levels. Wind speed, direction and
30 potential temperature profiles derived from a dropsonde launched at the end of the second



1 measurement leg (Fig. S2) are presented in Fig. 10a. Below 500 m, an almost neutrally
2 stratified boundary layer can be recognized, which is topped by a second neutrally stratified
3 layer between 500 m and 1800 m. Between 1800 m and 2000 m, the sounding measurements
4 show a thin and strong inversion ($\Delta\theta = 6\text{ K}$) coincident with the lower bound of the SAL,
5 which extends between 2000 m and 4100 m and exhibits a typical weak stratification. Along
6 these three layers, easterly winds with mean wind speed of 10 m s^{-1} are observed, while above
7 the SAL, the stratification increases, the wind speed reduces and the direction reverses. Based
8 on these measurements, the vertical profile of the Scorer parameter in its approximated form
9 (Fig. 10) was calculated. As in the previous case, these measurements were compared to the
10 DWL horizontal wind retrieval and the ECMWF ERA-Interim reanalysis results (not shown)
11 to confirm the representativeness of the measurements.

12 As expected, the calculated Scorer profile shows a thin layer of high Scorer parameter
13 corresponding to the strong inversion shown at 2000 m, upper bounded by a low Scorer
14 parameter layer which extends up to 3800 m and is associated with the weak stratification of
15 the SAL. Trapped waves at the density discontinuity associated with the inversion at 2000 m
16 are likely to occur in such conditions (Vosper, 2004; Sachsperger et al., 2015). Above the
17 SAL, the Scorer parameter increases due to a decrease in the wind speed and a stronger
18 stability of the atmosphere. The increase in the Scorer parameter can lead to the presence of
19 some wave leakage into the upper layers. Because the boundary layer is very weakly
20 stratified, the inverse Froude number is likely to be very close to zero. Based on the
21 dropsonde observations, the Brunt-Väisälä frequency at the boundary layer was estimated to
22 be $N = 0.0025\text{ s}^{-1}$ and the cross mountain wind speed approximately 12 m s^{-1} , which
23 together with a maximum island height of 340 m gives place to $F = 0.07$, suggesting a linear
24 flow condition.

25 These expectations were confirmed by the DWL observations, which showed the presence of
26 trapped lee waves on the lee side of Barbados (Fig. 11). The vertical winds measured by the
27 DWL during the first leg (Fig. 11a) show a strong updraft with 1.2 m s^{-1} on the north part of
28 Barbados, which is compatible with a measurement along a crest of the trapped waves. The
29 2nd leg (Fig 11b) supports this observation, showing a wave structure on the lee side, with a
30 wavelength of approximately 9 to 10 km and a vertical extension between 500 m and the top
31 of the SAL. Unfortunately the low aerosol load above the top of the SAL (4100 m) limits the
32 DWL coverage and the possibility to confirm the leakage by direct lidar measurements. The



1 maximum amplitude (up to 3 m s^{-1} peak to peak) of the waves is found at an altitude of around
2 2000 m, coinciding with high Scorer parameter layer, the temperature inversion and the
3 maxima in the wind shear altitude. Above and below the inversion, the wave amplitude
4 decrease, which is compatible with the evanescent wave regime $k^2 > l^2$ observed in the
5 Scorer parameter plot (Fig. 10b).

6 Although in this case the DWL measurement leg is long enough to resolve the spectra of the
7 observed waves below the top of the SAL, the low aerosol load limits the DWL coverage in
8 the upper part of the troposphere. For this reason, a wavelet transform was applied to the in-
9 situ vertical wind measurements of the 2nd, 3rd and 4th legs in order to determine the spectra of
10 the waves and whether or not there is leakage of the wave into upper layers (Fig. 12). The
11 spectra of the in-situ vertical wind measurements at 7745 m, corresponding to the 2nd leg (Fig.
12 11c and Fig. 12, upper panel), does not show signs of a spectral component with a wavelength
13 around 9 km, suggesting that this propagation mode does not leak into upper layers and that
14 the wave dissipation is dominated by the boundary layer absorption and dispersion (Durran et
15 al., 2015). This finding is compatible with the relatively short wavelength of the observed
16 wave, which lead to a strong vertical decay in the evanescent wave regime regions.

17 The spectral analysis corresponding to the 3rd and 4th legs (Fig. 12, mid and lower panel)
18 indicate the presence of a spectral component of the same wavelength than the observed by
19 the lidar during the 2nd leg (9.5 km), but with much lower amplitude. Although this change is
20 unexpected due to the short time difference between the 2nd leg (21:49 to 22:05 LT) and the
21 3rd leg (22:16 to 22:34 LT), relatively small changes in the atmospheric stability conditions
22 could have occurred in the time interval between both measurements, leading to a change in
23 the waves propagation condition.

24 Together with vertical wind measurements, calibrated backscatter coefficient profiles (Figs.
25 13a and 13b) were retrieved from the DWL measurements (Chouza et al., 2015) for the 1st
26 and 2nd leg. A three layer structure can be recognized in this case, with the marine boundary
27 layer below 500 m, a mixed layer between 500 m and 2000 m, and the SAL between 2000 m
28 and 4100 m. A wave structure can be identified in the boundary between the SAL and the
29 mixed layer at an altitude of 2000 m. Because the 3rd and 4th legs were flown at altitudes were
30 the gradient in the aerosol concentration was very low, no signature of waves is observed in
31 this case (Figs. 13c and 13d).



1 The backscatter coefficient and vertical wind corresponding to the boundary were the waves
2 were observed is displayed in Fig. 14. As for the previous case, a phase difference of 90
3 degrees is observed between both quantities, which is compatible with a no net flux condition.
4 Although in this particular case this feature was already observed by in-situ measurements in
5 the previous case study, the shown measurements provide an example of the possibilities
6 opened up by the simultaneous retrieval of vertical wind and calibrated backscatter coefficient
7 from a single instrument along a whole vertical transect. Based on the technique proposed by
8 Engelmann et al. (2008), the simultaneous retrieval of backscatter coefficient and vertical
9 wind can be used, under low humidity conditions, to retrieve aerosol vertical flux profiles.

10 **3.2.2 Large Eddy Simulations**

11 Large eddy simulations are performed with the All Scale Atmospheric Model (ASAM, Jähn et
12 al., 2015a) for the Barbados area. The model setup is described in Jähn et al. (2015b), where
13 the focus of the analysis lies on island effects on boundary layer modification, cloud
14 generation and vertical mixing of aerosols. In this study, the simulation results along the
15 measurement tracks are first compared with the DWL observations in order to provide further
16 validation of the model and setup. Then the whole simulation results are used to provide a
17 broader perspective of the context within which the measurements took place.

18 For the simulations, a model domain with a spatial extent of 102.4 x 102.4 km is chosen with
19 Barbados located at the domain center. The model top is at 5 km altitude. Grid spacings of
20 200 m (horizontally) and 50 m (vertically) are used and topographical data is obtained from
21 the Consortium for Spatial Information (CGIAR-CSI) Shuttle Radar Topography Mission
22 (SRTM) dataset (<http://srtm.csi.cgiar.org>) at 200 m resolution. The highest elevation of
23 Barbados is Mount Hillaby, 340 m above sea level. Due to the presence of a topographically
24 structured island surface in the domain center, the simulations are performed with open lateral
25 boundaries.

26 In order to generate inflow turbulence consistent with the upstream marine boundary layer
27 forcing, the newly developed turbulence generation method is applied. The model runs are
28 initialized with nighttime radiosonde data of the considered day and are integrated from 02:00
29 to 22:00 LT. Further details on the setup and comparison with the DWL can be found in Jähn
30 et al. (2015b).



1 In order to allow a qualitative comparison of the results from the LES with the measurements
2 from the DWL, plots of the simulated vertical wind speed on time periods similar to those
3 corresponding to the measurements are presented in Figs. 15 and 16. Figure 15 shows two
4 horizontal cuts of the vertical wind speed at 20:00 LT and 22:00 LT together with the flight
5 track of the Falcon corresponding to legs 1 and 2. The horizontal plane is located at an
6 altitude of 1975 m, coinciding with the temperature inversion observed by the in-situ
7 measurements and the maximum in the horizontal wind shear observed by the DWL, in-situ
8 and dropsonde measurements. Figure 16 displays the simulated vertical winds corresponding
9 to the 1st and 2nd legs flown by the Falcon (indicated in Fig. 15). The horizontal scales of the
10 plots were adjusted to simplify the comparison with the measurements presented in Fig. 11.

11 **3.2.3 Comparison of LES and DWL**

12 As can be seen in Figs. 15 and 16, the LES is able to reproduce the observations from the
13 DWL. A limited coverage over Barbados due to the presence of convective clouds is
14 compatible with the convective plumes observed in the simulations. Trapped waves with a
15 wavelength and extension similar to the lidar observations can be recognized on the lee side
16 of Barbados. The vertical cut presented in Fig. 16a shows an updraft above Barbados similar
17 the one shown in Fig. 11a and Fig. 15a shows that the vertical cut is located along a wave
18 crest. This simulation result provides support to the hypothesis presented in Sec. 4.1 to
19 explain the strong updraft observed above Barbados during the first measurement leg.

20 A wavelet transform was applied to the measured and simulated vertical wind speed in order
21 to provide a quantitative wavelength, amplitude and extension comparison of the simulated
22 and measured trapped waves. The measured data was interpolated in the same way as
23 described in Sec. 3, matching for this case, the spatial resolution of the LES (200 m). The
24 results of the wavelet transforms are presented in Fig. 17.

25 According to the wavelet analysis, the wavelength of the measured waves is approximately 9
26 km, while for the case of the LES the wavelength is approximately 7.5 km. The difference can
27 be attributed to different reasons such as small differences in the propagation direction of the
28 waves. As mentioned before, the LES is initialized with a constant wind speed direction equal
29 to 90°. This approximation can induce differences in the direction of propagation of the
30 waves, which in turn induce differences in the apparent wavelength of the measurements for
31 the same flight track.



1 While the amplitude of the simulated waves is quite similar at different altitudes, the DWL
2 measurements show a maximum in the amplitude at approximately 2000 m. This difference is
3 evident from the results of the wavelet analysis, calculated at the altitude of this maximum in
4 both cases. As explained in the previous section, the horizontal wind speed used for the
5 initialization of the LES is assumed constant between 0.7 km and 3 km. Because this
6 approximation neglects the strong shear measured at 2000 m, a difference between the
7 simulated and the measured vertical wind speed is expected at this altitude.

8

9 **4 Summary and conclusions**

10 In the first section of this work, a series of instrumental corrections required for the retrieval
11 of vertical winds from airborne DWL measurements were presented. The difference of almost
12 two orders of magnitude between the platform speed and the measured vertical wind speed,
13 together with the varying aircraft orientation during the flight, transforms the retrieval of
14 vertical winds in a challenging problem. Although no control of the lidar pointing direction
15 was active during the vertical wind measurements, the use of horizontal wind from
16 dropsondes and in-situ measurements proved to be useful to partially compensate the effects
17 of the horizontal wind component projection. The use of conical scanning pattern
18 measurements and the recalculation of the lidar mounting angle based on the ground return
19 speed and distance previous to the vertical wind measurements proved to be useful to reduce
20 the systematic error, especially after a change in the flight altitude. The measurement
21 uncertainties were estimated based on two different techniques. The estimated systematic
22 error, based one measurement case, was -0.05 ms^{-1} , while the random error was between 0.1
23 ms^{-1} and 0.16 ms^{-1} depending on the technique used for the estimation.

24 The described methods were applied to retrieve vertical winds corresponding to two
25 SALTRACE research flights, one in the Cape Verde region and a second one in Barbados.
26 The measurements revealed the presence of island induced gravity waves in both cases.
27 Vertical profiles of temperature, wind and humidity obtained from in-situ and dropsonde
28 measurements were used to calculate a Scorer parameter profile for each measurement case.
29 The wavelength and the vertical extension of the trapped waves observed from the DWL
30 measurements in the Cape Verde case study were in coincidence with the retrieved Scorer
31 parameter profile. The spatial extension, amplitude and wavelength retrieved from the in-situ
32 vertical wind measurements provided an independent validation for the DWL observation. A



1 second independent observation of the particle number concentration provided an additional
2 confirmation.

3 Although for the second case study the in-situ measurement did not show the waves observed
4 by the DWL in a previous leg, the results of the ASAM model support the lidar observations.
5 The model was able to reproduce the generation of waves in the lee side of the island and
6 provided a context to the lidar observations, which are limited to two dimensional vertical
7 cuts. The amplitude and wavelength of the simulated waves were lower than the observed
8 ones. This can be explained by the simplifications adopted in the horizontal wind profiles
9 used to initialize the model, which did not reproduce the strong shears observed in the
10 dropsondes and in-situ measurements.

11

12 **Acknowledgements**

13 This work was funded by the Helmholtz Association under grant number VH-NG-606
14 (Helmholtz-Hochschul-Nachwuchsforschergruppe AerCARE). The SALTRACE campaign
15 was mainly funded by the Helmholtz Association, DLR, LMU and TROPOS. The
16 SALTRACE flights on Cape Verde were funded through the DLR-internal project VolcATS
17 (Volcanic ash impact on the Air Transport System). DLR Falcon aircraft in-situ data was
18 processed by the DLR Flight Experiment. The first author thanks the German Academic
19 Exchange Service (DAAD) for the financial support.

20



1 **References**

- 2 Alexander, M. J. and Grimsdell, A. W.: Seasonal cycle of orographic gravity wave occurrence
3 above small islands in the Southern Hemisphere: Implications for effects on the general
4 circulation, *J. Geophys. Res. Atmos.*, 118, 11,589–11,599, doi:10.1002/2013JD020526, 2013.
- 5 Amirault, C., DiMarzio C.: Precision pointing using a dual-wedge scanner, *Appl. Opt.*, 24,
6 1302-1308, 1985.
- 7 Baik, J.: Response of a Stably Stratified Atmosphere to Low-Level Heating— An Application
8 to the Heat Island Problem, *J. Appl. Meteor.*, 31, 291–303, doi: 10.1175/1520-
9 0450(1992)031<0291:ROASSA>2.0.CO;2, 1992.
- 10 Baines, J. and Hoinka, K. P.: Stratified Flow over Two-Dimensional Topography in Fluid of
11 Infinite Depth: A Laboratory Simulation, *J. Atmos. Sci.*, 42, 1614–1630, doi:
12 [http://dx.doi.org/10.1175/1520-0469\(1985\)042<1614:SFOTDT>2.0.CO;2](http://dx.doi.org/10.1175/1520-0469(1985)042<1614:SFOTDT>2.0.CO;2), 1985.
- 13 Bluman, W. and Hart, J. E.: Airborne Doppler Lidar Wind Field Measurements of Waves in
14 the Lee of Mount Shasta, *J. Atmos. Sci.*, 45, 1571–1583, doi: 10.1175/1520-
15 0469(1988)045<1571:ADLWFM>2.0.CO;2, 1988.
- 16 Bosart, B., Lee, W., Wakimoto, R.: Procedures to Improve the Accuracy of Airborne Doppler
17 Radar Data. *J. Atmos. Oceanic Technol.*, 19, 322–339, doi: 10.1175/1520-0426-19.3.322,
18 2002.
- 19 Chouza, F., Reitebuch, O., Groß, S., Rahm, S., Freudenthaler, V., Toledano, C., and
20 Weinzierl, B.: Retrieval of aerosol backscatter and extinction from airborne coherent Doppler
21 wind lidar measurements, *Atmos. Meas. Tech.*, 8, 2909-2926, doi:10.5194/amt-8-2909-2015,
22 2015.
- 23 Cui, Z., Blyth, A. M., Bower, K. N., Crosier, J., and Choulaton, T.: Aircraft measurements of
24 wave clouds, *Atmos. Chem. Phys.*, 12, 9881-9892, doi:10.5194/acp-12-9881-2012, 2012.
- 25 De Wekker, S. F. J., Godwin, K. S., Emmitt, G. D., Greco, S.: Airborne Doppler Lidar
26 Measurements of Valley Flows in Complex Coastal Terrain, *J. Appl. Meteor. Climatol.*, 51,
27 1558–1574, doi: 10.1175/JAMC-D-10-05034.1, 2012.
- 28 Durran, D. R.: Mountain waves and downslope winds, in: *Atmospheric Process over Complex*
29 *Terrain*, Blumen, W., American Meteorological Society, Boston, 59–81, 1990.



- 1 Durrán, D. R., Hills, M. O. G., Blossey, P. N.: The Dissipation of Trapped Lee Waves. Part I:
2 Leakage of Inviscid Waves into the Stratosphere, *J. Atmos. Sci.*, 72, 1569–1584, doi:
3 <http://dx.doi.org/10.1175/JAS-D-14-0238.1>, 2015.
- 4 Ehard, B., Kaifler, B., Kaifler, N., and Rapp, M.: Evaluation of methods for gravity wave
5 extraction from middle-atmospheric lidar temperature measurements, *Atmos. Meas. Tech.*, 8,
6 4645–4655, doi:10.5194/amt-8-4645-2015, 2015.
- 7 Emmitt, G. D. and Godwin, K.: Advanced airborne Doppler Wind Lidar signal processing for
8 observations in complex terrain, *Proc. SPIE 9246, Lidar Technologies, Techniques, and*
9 *Measurements for Atmospheric Remote Sensing X*, 924609, doi:10.1117/12.2068226, 2014.
- 10 Engelmann, R., Wandinger, U., Ansmann, A., Müller, D., Žeromskis, E., Althausen, D. and
11 Wehner, B.: Lidar Observations of the Vertical Aerosol Flux in the Planetary Boundary
12 Layer. *J. Atmos. Oceanic Technol.*, 25, 1296–1306, doi:
13 <http://dx.doi.org/10.1175/2007JTECHA967.1>, 2008.
- 14 Engelmann, R., Ansmann, A., Horn, S., Seifert, P., Althausen, D., Tesche, M., Esselborn, M.,
15 Fruntke, J., Lieke, K., Freudenthaler, V. and Groß, S.: Doppler lidar studies of heat island
16 effects on vertical mixing of aerosols during SAMUM–2, *Tellus B*, 63, 448–458.
17 doi: 10.1111/j.1600-0889.2011.00552.x, 2011.
- 18 Frehlich, R.: Errors for Space-Based Doppler Lidar Wind Measurements: Definition,
19 Performance, and Verification, *J. Atmos. Oceanic Technol.*, 18, 1749–1772, 2001.
- 20 Georgelin, M. and Lott, F.: On the Transfer of Momentum by Trapped Lee Waves: Case of
21 the IOP 3 of PYREX, *J. Atmos. Sci.*, 58, 3563–3580, doi: [http://dx.doi.org/10.1175/1520-](http://dx.doi.org/10.1175/1520-0469(2001)058<3563:OTTOMB>2.0.CO;2)
22 [0469\(2001\)058<3563:OTTOMB>2.0.CO;2](http://dx.doi.org/10.1175/1520-0469(2001)058<3563:OTTOMB>2.0.CO;2), 2001.
- 23 Grewal, M. S., Weill, L. R. and Andrews, A. P.: Appendix C: Coordinate Transformations, in:
24 *Global Positioning Systems, Inertial Navigation, and Integration*, Second Edition, John Wiley
25 & Sons, Inc., Hoboken, NJ, USA, 456–501, doi: 10.1002/9780470099728.app3, 2007.
- 26 Henderson, S.W., Suni, P. J M, Hale, C.P., Hannon, S.M., Magee, J.R., Bruns, D.L., Yuen,
27 E.H.: Coherent laser radar at 2 μm using solid-state lasers, *IEEE Transactions on Geoscience*
28 *and Remote Sensing*, 31.1, 4–15, 1993.



- 1 Jähn, M., Knoth, O., König, M., and Vogelsberg, U.: Asam v2.7: a compressible atmospheric
2 model with a cartesian cut cell approach, *Geoscientific Model Development*, 8(2):317–340,
3 2015a.
- 4 Jähn, M., Muñoz Esparza, D., Chouza, F., and Reitebuch, O.: Investigations of boundary layer
5 structure, cloud characteristics and vertical mixing of aerosols at Barbados with large eddy
6 simulations, *Atmospheric Chemistry and Physics Discussions*, 15(16):22637–22699, 2015b.
- 7 Kavaya, M. J., Beyon, J. Y., Koch, G. J., Petros, M., Petzar, P. J., Singh, U. N., Trieu, B. C.,
8 Yu, J.: The Doppler Aerosol Wind (DAWN) Airborne, Wind-Profiling Coherent-Detection
9 Lidar System: Overview and Preliminary Flight Results, *J. Atmos. Oceanic Technol.*, 31,
10 826–842, doi: 10.1175/JTECH-D-12-00274.1, 2014.
- 11 Käsler, Y., Rahm, S., Simmet, R., Kühn, M.: Wake measurements of a multi-MW wind
12 turbine with coherent long-range pulsed doppler wind lidar, *Journal of Atmospheric and*
13 *Oceanic Technology*, 27, 1529-1532, 2010.
- 14 Kiemle, C., Ehret, G., Fix, A., Wirth, M., Poberaj, G., Brewer, W. A., Hardesty, R. M., Senff,
15 C., LeMone, M. A.: Latent Heat Flux Profiles from Collocated Airborne Water Vapor and
16 Wind Lidars during IHOP_2002, *J. Atmos. Oceanic Technol.*, 24, 627–639,
17 doi:10.1175/JTECH1997.1, 2007.
- 18 Kiemle, C., Wirth, M., Fix, A., Rahm, S., Corsmeier, U., Di Girolamo, P.: Latent heat flux
19 measurements over complex terrain by airborne water vapour and wind lidars. *Q.J.R.*
20 *Meteorol. Soc.*, 137, 190–203, doi: 10.1002/qj.757, 2011.
- 21 Kirkwood, S., Mihalikova, M., Rao, T. N., and Satheesan, K.: Turbulence associated with
22 mountain waves over Northern Scandinavia – a case study using the ESRAD VHF radar and
23 the WRF mesoscale model, *Atmos. Chem. Phys.*, 10, 3583-3599, doi:10.5194/acp-10-3583-
24 2010, 2010.
- 25 Köpp, F., Rahm, S., Smalikho, I.: Characterization of Aircraft Wake Vortices by 2- μ m Pulsed
26 Doppler Lidar, *Journal of Atmospheric and Oceanic Technology*, 21, 194–206, 2004.
- 27 Kühnlein, C., Dörnbrack, A., Weissmann, M.: High-Resolution Doppler Lidar Observations
28 of Transient Downslope Flows and Rotors. *Mon. Wea. Rev.*, 141, 3257–3272, doi:
29 <http://dx.doi.org/10.1175/MWR-D-12-00260.1>, 2013.



- 1 O'Connor, E. J., Illingworth, A. J., Brooks, I. M., Westbrook, C. D., Hogan, R. J., Davies, F.,
2 Brooks, B. J.: A Method for Estimating the Turbulent Kinetic Energy Dissipation Rate from a
3 Vertically Pointing Doppler Lidar, and Independent Evaluation from Balloon-Borne In Situ
4 Measurements, *J. Atmos. Oceanic Technol.*, 27, 1652–1664, doi:
5 10.1175/2010JTECHA1455.1, 2010.
- 6 Prospero, J. M.: Long-range transport of mineral dust in the global atmosphere: Impact of
7 African dust on the environment of the southeastern United States, *Proc. Natl. Acad. Sci. U.*
8 *S. A.*, 96, 3396–3403, 1999.
- 9 Prospero, J.M., Mayol-Bracero, O. L.: Understanding the Transport and Impact of African
10 Dust on the Caribbean Basin, *Bull. Amer. Meteor. Soc.*, 94, 1329–1337, doi:
11 <http://dx.doi.org/10.1175/BAMS-D-12-00142.1>, 2013.
- 12 Rahm, R., Smalikho, I., Köpp, F.: Characterization of Aircraft Wake Vortices by Airborne
13 Coherent Doppler Lidar, *Journal of Aircraft*, 44, 799–805, 2007.
- 14 Reitebuch, O.: Wind Lidar for Atmospheric Research, in: *Atmospheric Physics*, Schumann,
15 U., Springer, Berlin Heidelberg, 487–507, 2012.
- 16 Reitebuch, O., Werner, C., Leike, I., Delville, P., Flamant, P. H., Cress, A., Engelbart, D.:
17 Experimental validation of wind profiling performed by the airborne 10- μ m heterodyne
18 Doppler Lidar WIND, *Journal of Atmospheric and Oceanic Technology*, 18, 1331–1344,
19 2001.
- 20 Reitebuch, O., H. Volkert, C. Werner, A. Dabas, P. Delville, P. Drobinski, P. H. Flamant, and
21 E. Richard: Determination of air flow across the Alpine ridge by a combination of airborne
22 Doppler lidar, routine radio-sounding, and numerical simulation. *Quart. J. Roy. Meteor. Soc.*,
23 129, 715–728, 2003.
- 24 Sachsperger, J., Serafin, S., Grubišić, V., Lee Waves on the Boundary-Layer Inversion and
25 Their Dependence on Free-Atmospheric Stability, *Front. Earth Sci.*, 3:70, doi:
26 10.3389/feart.2015.00070, 2015.
- 27 Savijärvi, H. and Matthews, S.: Flow over Small Heat Islands: A Numerical Sensitivity Study,
28 *J. Atmos. Sci.*, 61, 859–868, doi: 10.1175/1520-0469(2004)061<0859:FOSHIA>2.0.CO;2,
29 2004.



- 1 Scorer, R. S.: Theory of waves in the lee of mountains, Q.J.R. Meteorol. Soc., 75, 41–56,
2 doi: 10.1002/qj.49707532308, 1949.
- 3 Smith, R. B.: Linear theory of stratified hydrostatic flow past an isolated obstacle, Tellus, 32,
4 348–364, 1980.
- 5 Smith, R. B., Skubis, S., Dolye, J. D., Broad, A. and Volkert, H.: Mountain waves over Mont
6 Blanc: Influence of a stagnant boundary layer, J. Atmos. Sci., 59, 2073–2092, 2002.
- 7 Torrence, C. and Compo, G. P.: A practical guide to wavelet analysis, Bull. Amer. Meteor.
8 Soc., 79, 61–78, 1998.
- 9 Vosper, S. B., Inversion effects on mountain lee waves, Q.J.R. Meteorol. Soc., 130: 1723–
10 1748. doi:10.1256/qj.03.63, 2004.
- 11 Weinzierl, B., Sauer, D., Esselborn, M., Petzold, A., Veira, A., Rose, M., Mund, S., Wirth,
12 M., Ansmann, A., Tesche, M., Groß, S. and Freudenthaler, V.: Microphysical and optical
13 properties of dust and tropical biomass burning aerosol layers in the Cape Verde region—an
14 overview of the airborne in situ and lidar measurements during SAMUM-2, Tellus B,
15 63, 589–618, doi: 10.1111/j.1600-0889.2011.00566.x, 2011.
- 16 Weissmann, M., Busen, R., Dörnbrack, A., Rahm, S., Reitebuch, O.: Targeted observations
17 with an airborne wind lidar, Journal of Atmospheric and Oceanic Technology, 22, 1706-1719,
18 2005.
- 19 Woods, B. K. and Smith, R. B.: Energy Flux and Wavelet Diagnostics of Secondary
20 Mountain Waves, J. Atmos. Sci., 67, 3721–3738, doi: 10.1175/2009JAS3285.1, 2010.

21

22



1 Table 1. Key parameters of the DWL

Laser	Laser type	Solid-state Tm:LuAG
	Operation wavelength	2.02254 μm
	Laser energy	1-2 mJ
	Repetition rate	500 Hz
	Pulse length (FWHM)	400 ns
Transceiver	Telescope type	Off-axis
	Telescope diameter	10.8 cm
	Transmitted polarization	Circular
	Detected polarization	Co-polarized
Scanner	Type	Double wedge
	Material	Fused silica
Data acquisition	Sampling rate	500 MHz
	Resolution	8 bits
	Mode	Single shot acquisition

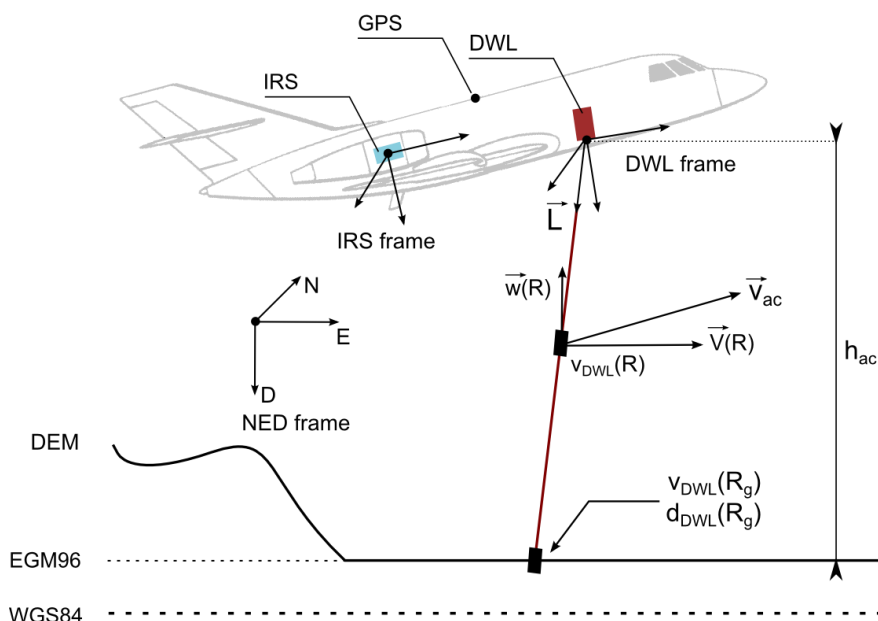
2
3



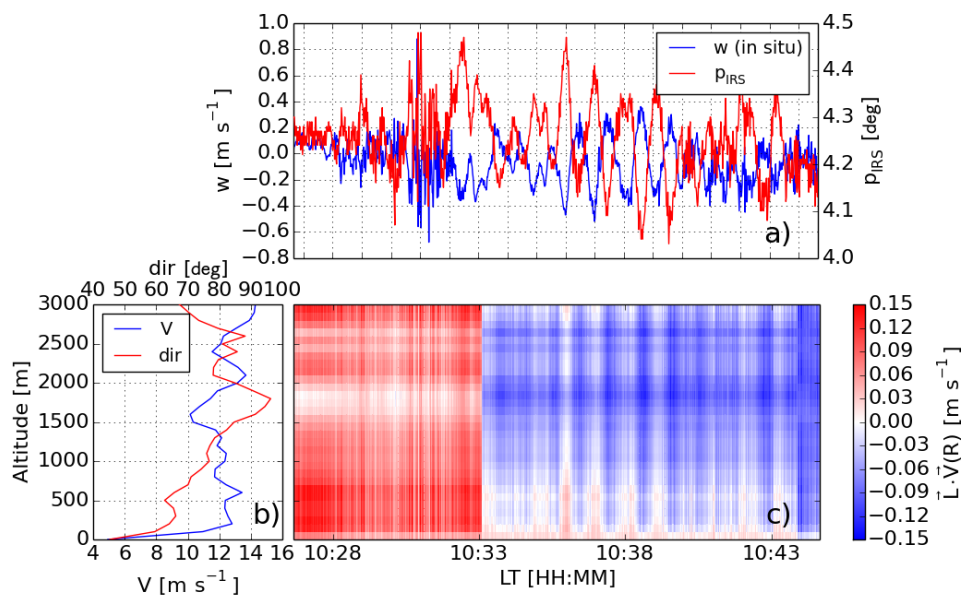
1 Table 2. Estimated lidar mounting angles. The first row of each flight corresponds to the
 2 retrieved mounting angle using distance and speed measurements, while the second and third
 3 rows correspond to the use of only distance or speed respectively.

Date	Sea surface points	Land surface points	Estimated mounting angle [°]		
	(Distance method)	(Speed method)	Γ_{DWL}	ρ_{DWL}	γ_{DWL}
	58	304	0.91	-2.09	1.64
12.06.13	58	-	0.82	-2.14	3.23
	-	304	0.66	-2.10	1.61
	277	500	1.00	-2.07	1.63
18.06.13	277	-	1.31	-2.13	-1.94
	-	500	0.11	-2.11	1.55
	60	136	0.99	-2.07	1.63
13.07.13	60	-	1.09	-2.11	-0.04
	-	136	0.89	-2.08	1.63
	269	161	0.80	-2.13	1.64
14.07.13	269	-	0.20	-2.33	11.52
	-	161	0.66	-2.14	1.64
	59	397	0.92	-2.07	1.69
14.07.13	59	-	1.13	-2.04	1.82
	-	397	0.88	-2.07	1.69
	5403	3449	0.98	-2.08	1.62
All flights	5403	-	0.99	-2.11	1.37
	-	3449	1.00	-2.08	1.62

4



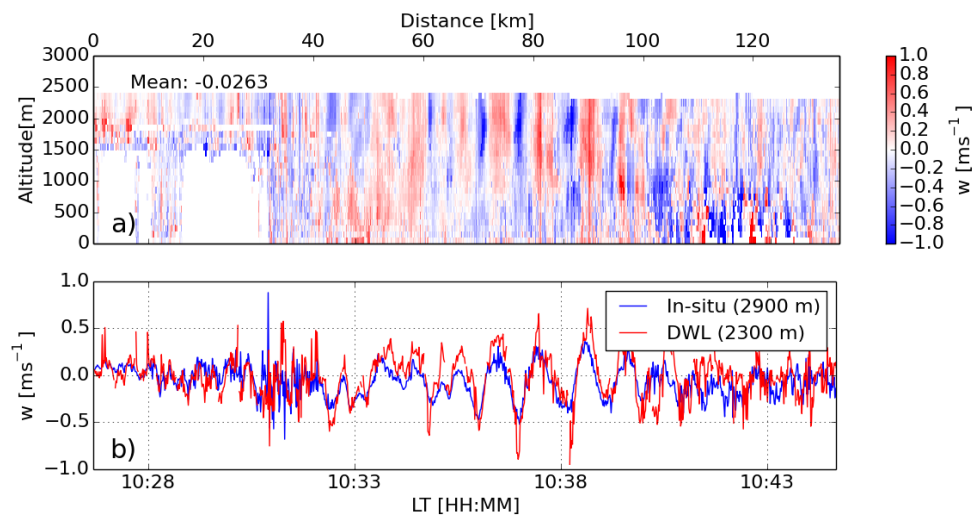
1 WGS84
 2 Figure 1. Scheme with the different reference frames and magnitudes involved in the vertical
 3 wind retrieval calculations. The DWL frame is a reference frame fixed to the DWL
 4 transceiver head, the IRS frame is a reference frame fixed to aircraft inertial reference system
 5 (IRS) and the NED (North-East-Down) frame is an Earth reference frame for which the x axis
 6 is pointing northwards, the y axis is pointing eastwards and the z axis completes the right
 7 handed reference system pointing downwards, parallel to the norm of a plane tangential to the
 8 Earth reference ellipsoid. \vec{L} is a unit vector that represents the DWL line of sight (LOS), \vec{v}_{ac} is
 9 the aircraft speed, \vec{V} and \vec{w} are the horizontal and vertical wind speed respectively in a range
 10 R from the lidar, v_{DWL} is the relative speed measured by the DWL, h_{ac} is the aircraft altitude
 11 about ground level and R_g is the range between the lidar and the ground. WGS84 is the World
 12 Geodetic System 1984 standard used by the GPS system, while EGM96 is the Earth
 13 Gravitational Model 1996 used for correction.
 14



1

2 Figure 2. a) Vertical wind speed (blue) measured by the aircraft in-situ sensors at 2900 m,
 3 together with the aircraft pitch (red). b) Average of the horizontal wind speed (blue) and
 4 direction (red) retrieved by the DWL during a previous leg flown along the same track. c)
 5 Projection of the horizontal wind speed to the DWL LOS due to changes in the aircraft
 6 orientation. At 10:33 LT the DWL LOS was changed by the operator in-flight to reduce the
 7 horizontal wind projection.

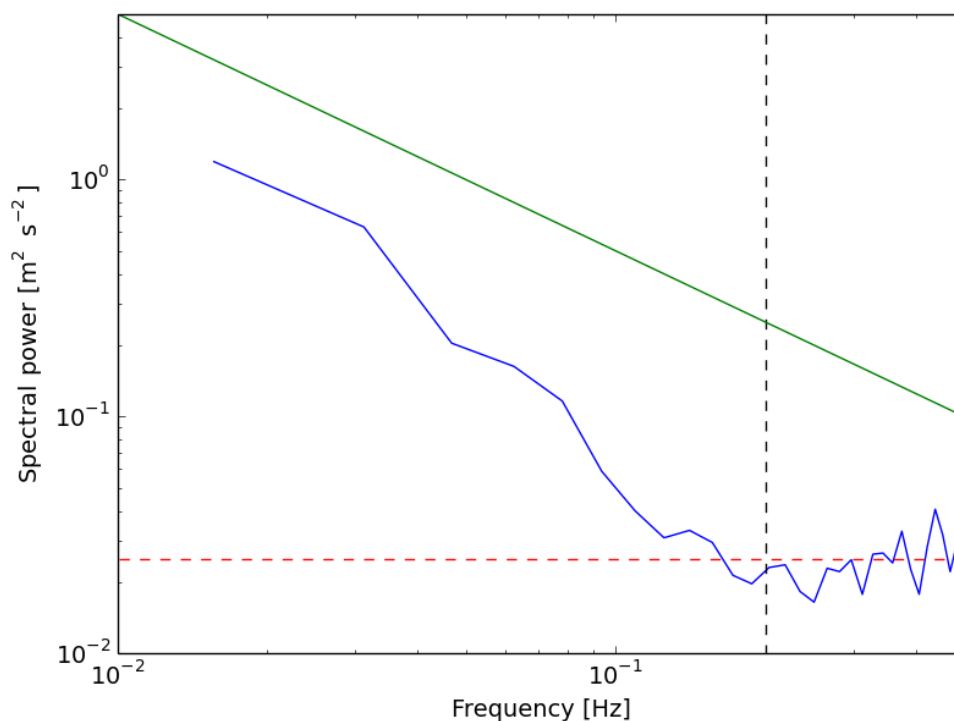
8



1

2 Figure 3. a) DWL vertical wind speed retrieval for a leg flown on 20 June 13 between 10:31
3 and 10:45 LT. Positive (red) indicates upward winds and negative (blue) indicates downward
4 winds. Between 10:27 LT and 10:31 LT the DWL coverage is limited due to the presence of
5 clouds (white regions below 1500 m). b) Comparison between the vertical wind retrieved by
6 the Falcon 20 (blue) for an altitude of 2900 m and the DWL retrieval (red) for an altitude of
7 2300 m.

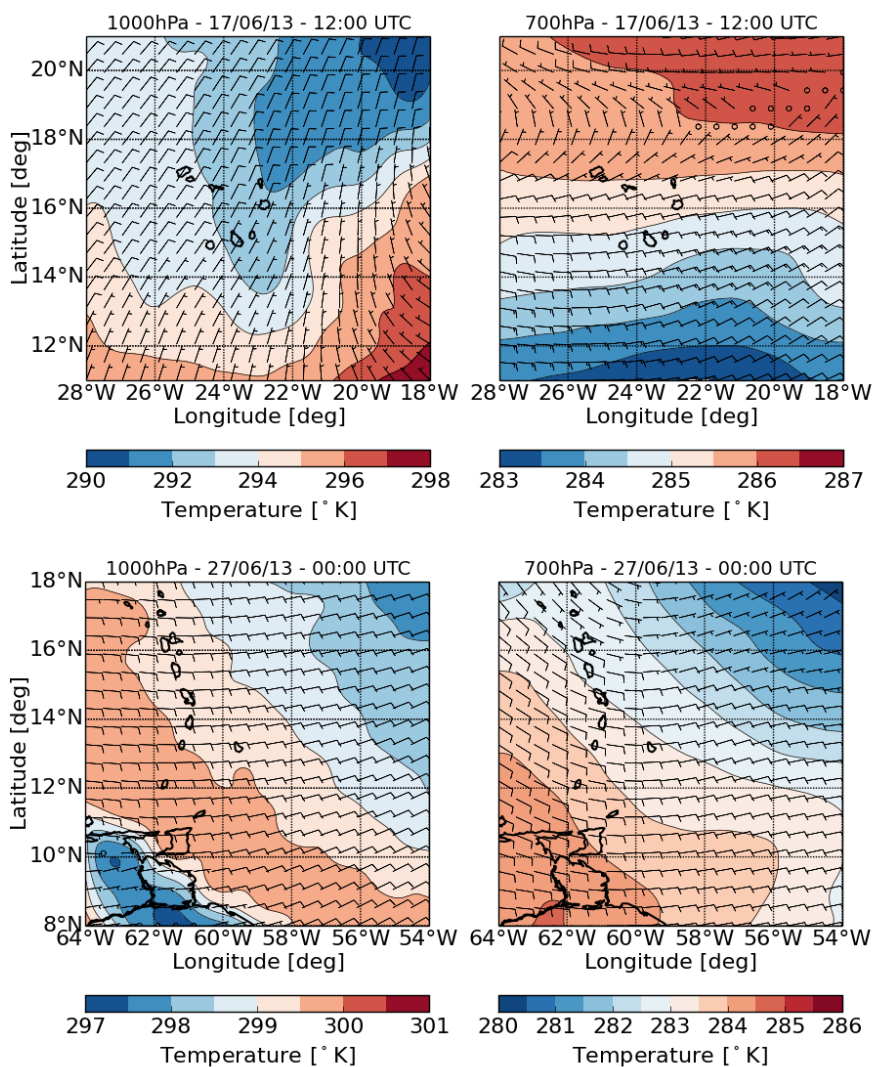
8



1

2 Figure 4. Spectral power for the DWL measured vertical wind speed during the flight on 20
3 June 2013, between 10:31 and 10:45 LT and for an altitude of 2300 m (solid, blue). The
4 expected spectral behavior according to the Kolmogorov's $-5/3$ law (green line), the noise
5 frequency threshold (black, dotted) and the derived noise floor for the DWL (red, dotted) are
6 shown.

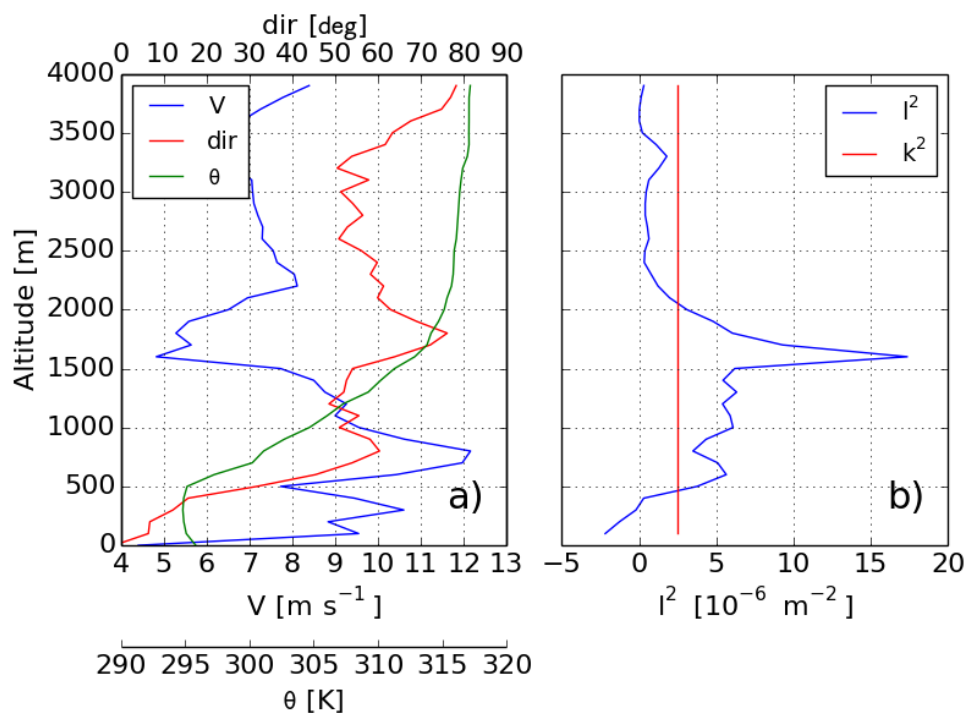
7



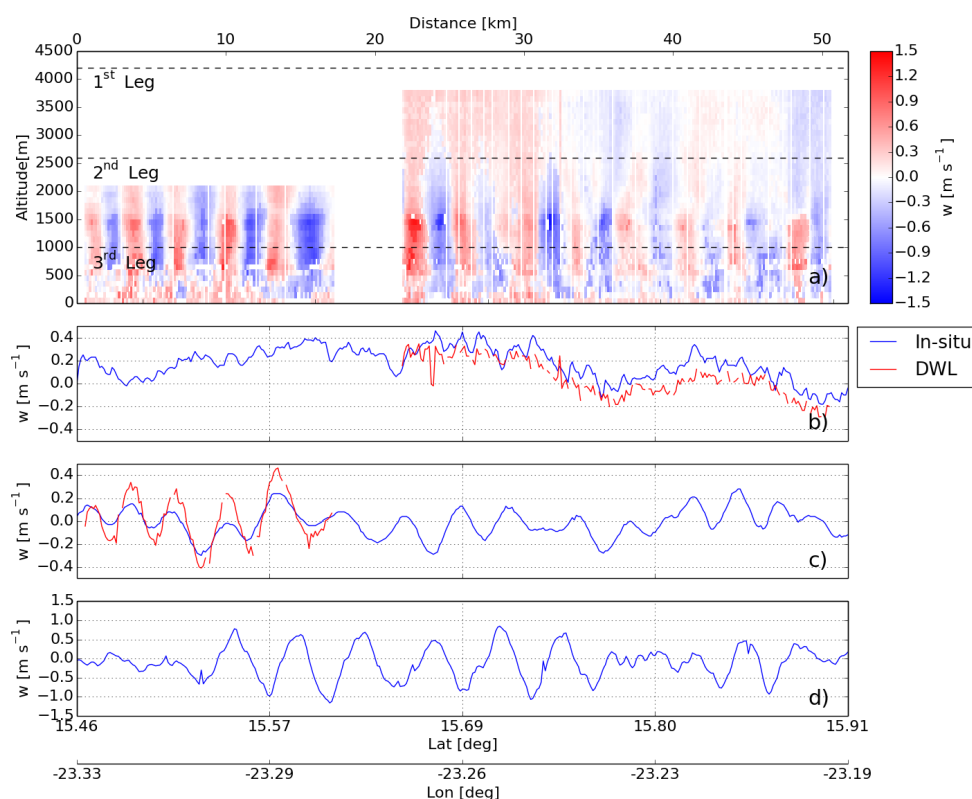
1

2 Figure 5. Synoptic conditions derived from the ECMWF ERA-Interim reanalysis over the
3 Cape Verde islands (upper panels) and Barbados (lower panels) for the 17 June 2013 and 27
4 June 2013 respectively. Wind vectors (barbs, in m s^{-1}) and temperature (in $^{\circ}\text{K}$) are shown.

5



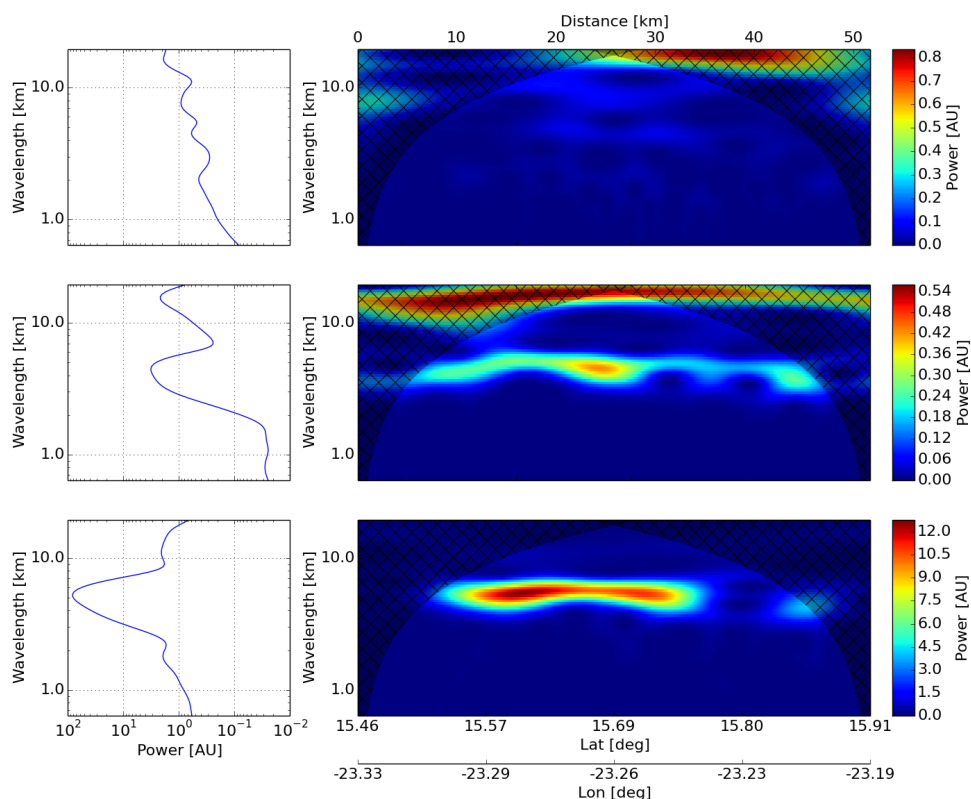
1
2 Figure 6. a) Horizontal wind speed (blue), wind direction (red) and potential temperature
3 (green) measured by the Falcon in-situ sensors during take-off (10:06 to 10:14 LT). b)
4 Derived Scorer parameter (blue) and approximate wave number corresponding to the
5 observed waves (red).
6



1

2 Figure 7. a) Retrieved vertical wind speed by the DWL as a function of the latitude and
3 longitude from legs 1 (10:21 to 10:25 LT) and 2 (10:43 to 10:46 LT), together with the flight
4 levels corresponding to the legs 1, 2 and 3 (11:10 to 11:16 LT) (dashed lines). b, c, d) In-situ
5 vertical wind speed corresponding to the legs 1, 2 and 3 (blue line) together with the
6 measured wind corresponding to the uppermost range gate measured on each leg (red line).

7

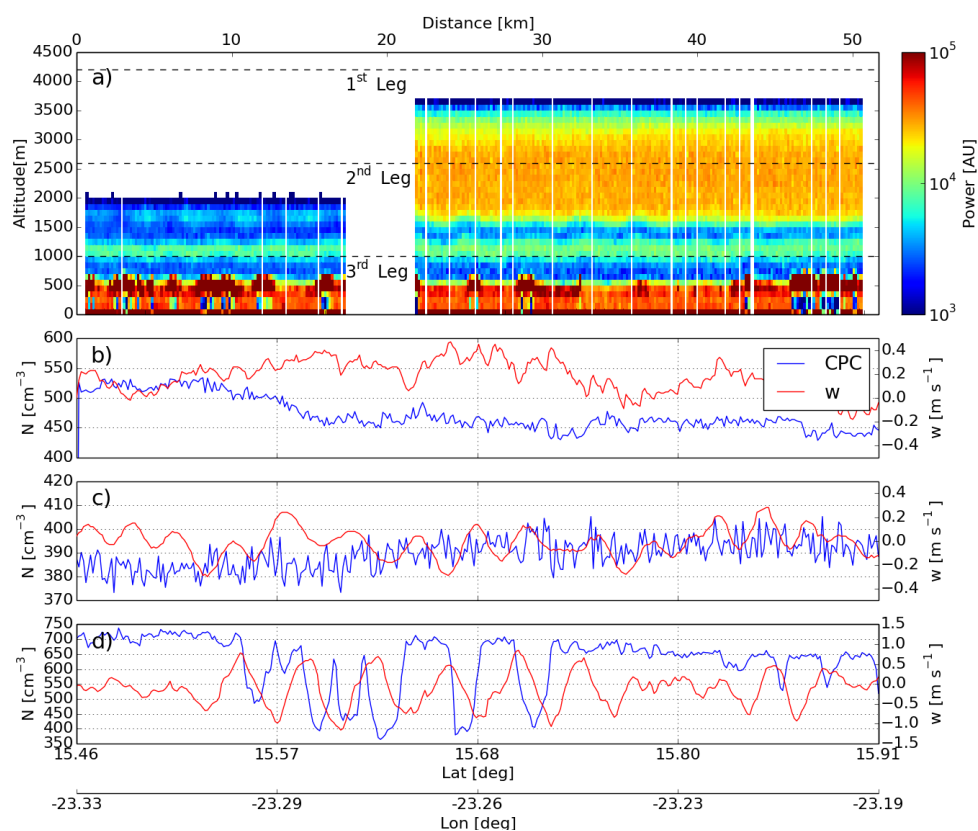


1

2 Figure 8. In-situ vertical wind wavelet analysis corresponding to the three legs flown on 17
3 June: 1st leg (upper panels), 2nd leg (mid panels) and 3rd leg (lower panels). The hatched areas
4 indicate the cone of influence. The left panels show the average power for each wavelength.

5

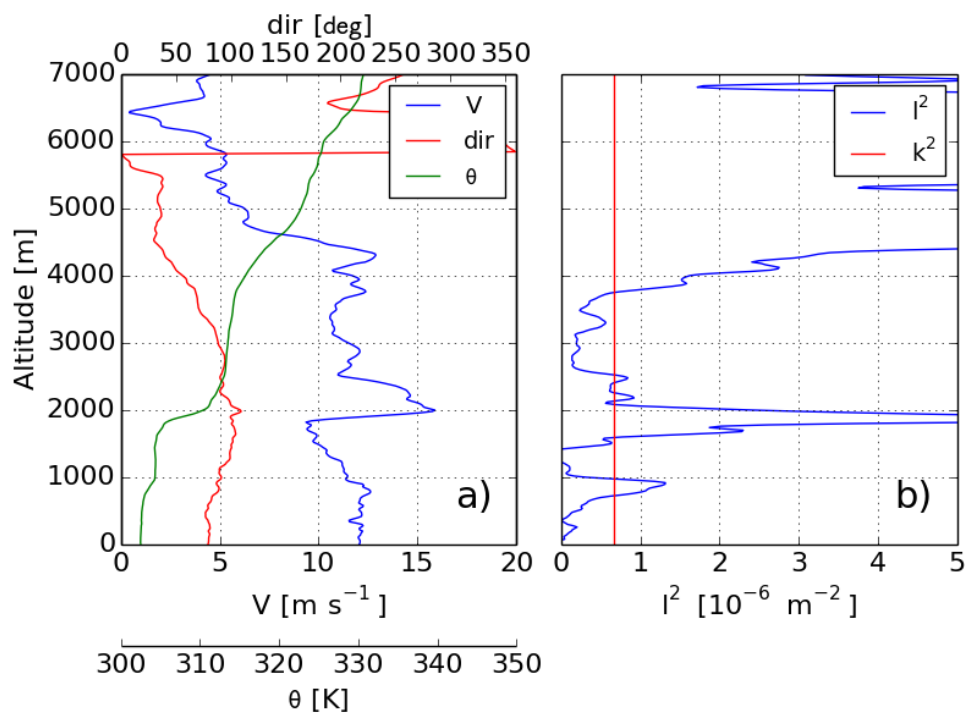
6



1

2 Figure 9. a) Retrieved range corrected backscatter power by the DWL as a function of the
3 latitude and longitude from legs 1 and 2, together with the flight levels corresponding to the
4 legs 1, 2 and 3 (dashed lines). b, c, d) In-situ CPC measurements (blue line) corresponding to
5 the legs 1, 2 and 3 together with the in-situ measured vertical wind (red line).

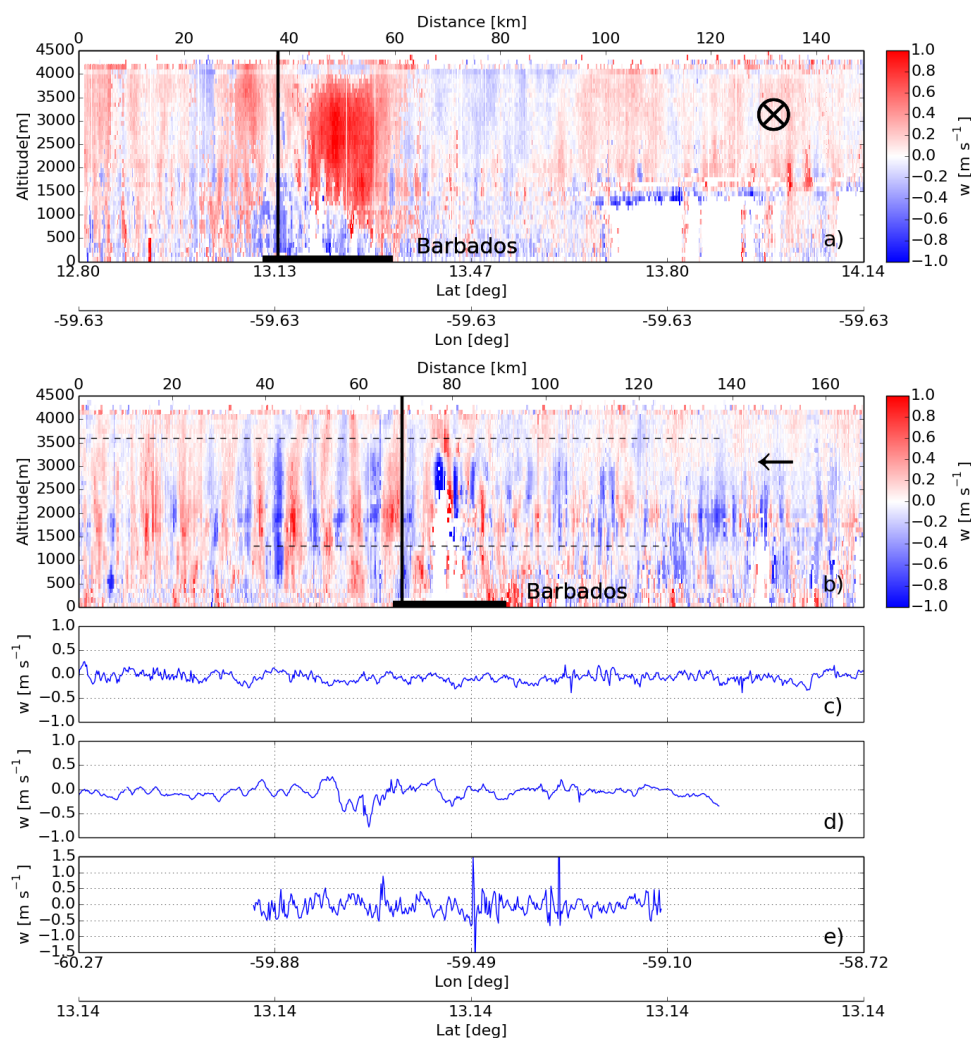
6



1

2 Figure 10. a) Horizontal wind speed (blue), wind direction (red) and potential temperature
3 (green) measured by a dropsonde launched at (26.6.13 - 22:05 LT). b) Derived Scorer
4 parameter (blue) and approximate wave number corresponding to the observed waves (red).

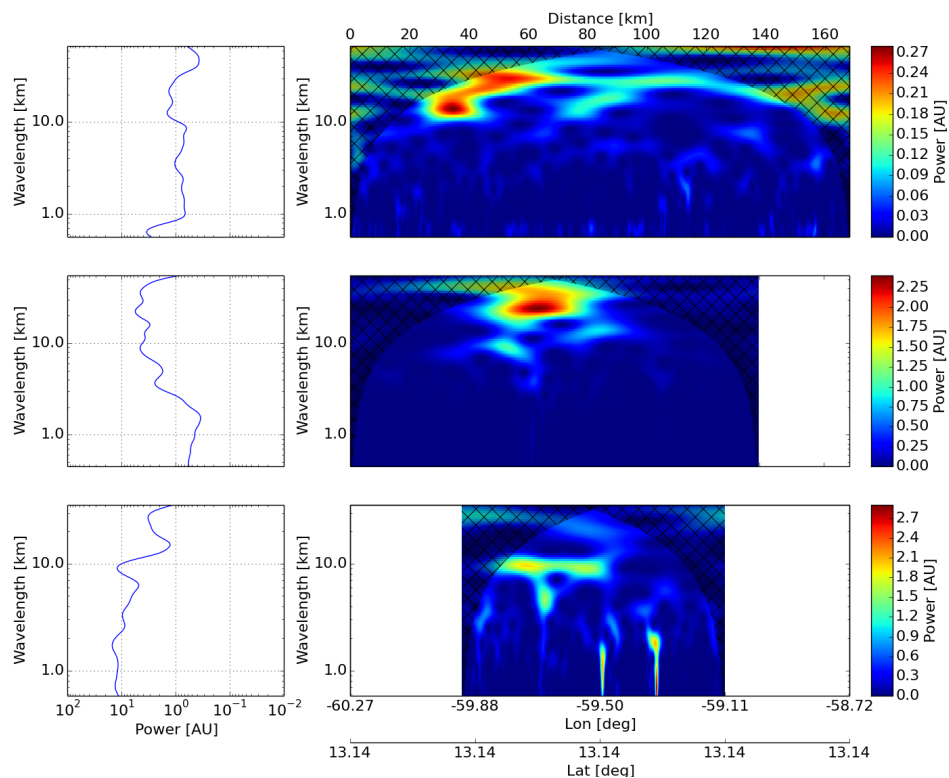
5



1

2 Figure 11. a) Retrieved vertical wind speed by the DWL as a function of the latitude and
 3 longitude from leg 1 (19:53 to 20:06 LT), together with the latitude at which legs 2 (21:49 to
 4 22:05 LT), 3 (22:16 to 22:34 LT) and 4 were flown (22:46 to 23:01 LT) (solid line). b)
 5 Retrieved vertical wind speed by the DWL as a function of the latitude and longitude from leg
 6 2, the intersection position with the 1st leg (solid line) and the legs 3 and 4 are shown (dashed
 7 line). c, d, e) In-situ vertical wind speed corresponding to the legs 2, 3 and 4. The average
 8 wind inflow direction is indicated on the upper-right corner of panels a) and b). Barbados
 9 indicated in both plots with a horizontal solid black line.

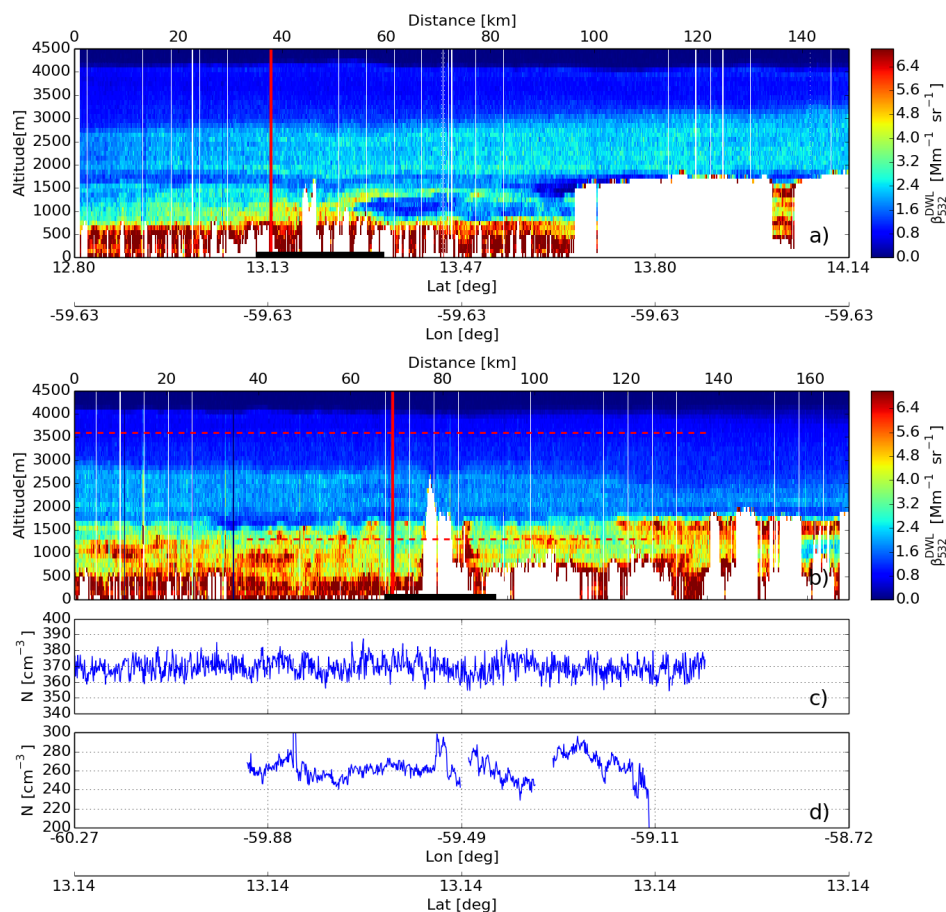
10



1

2 Figure 12. In-situ vertical wind wavelet analysis corresponding to three legs flown on 26
3 June: 2nd leg (upper panels), 3rd leg (mid panels) and 4th leg (lower panels). The hatched areas
4 indicate the cone of influence. The left panels show the average power for each wavelength.

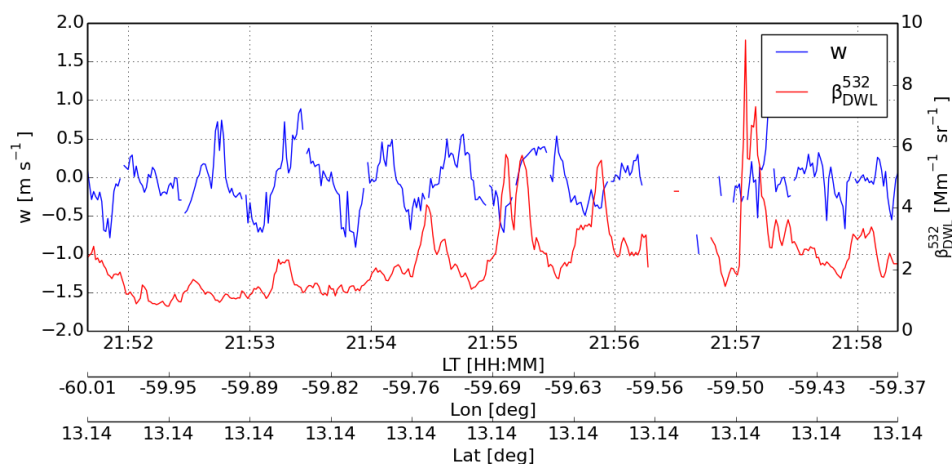
5



1

2 Figure 13. a) Retrieved backscatter coefficient by the DWL as a function of the latitude and
 3 longitude from leg 1, together with the latitude at which legs 2, 3 and 4 were flown (solid line,
 4 red). b) Retrieved backscatter coefficient by the DWL as a function of the latitude and
 5 longitude from leg 2, the intersection position with the 1st leg (solid line, red) and the legs 3
 6 and 4 are shown (dashed line., red). c, d) In-situ CPC measurements corresponding to the legs
 7 3 and 4. The white color indicates regions where no atmospheric signal is available (e.g., below
 8 clouds, unseeded laser operation). Barbados indicated in both plots with a horizontal solid
 9 black line.

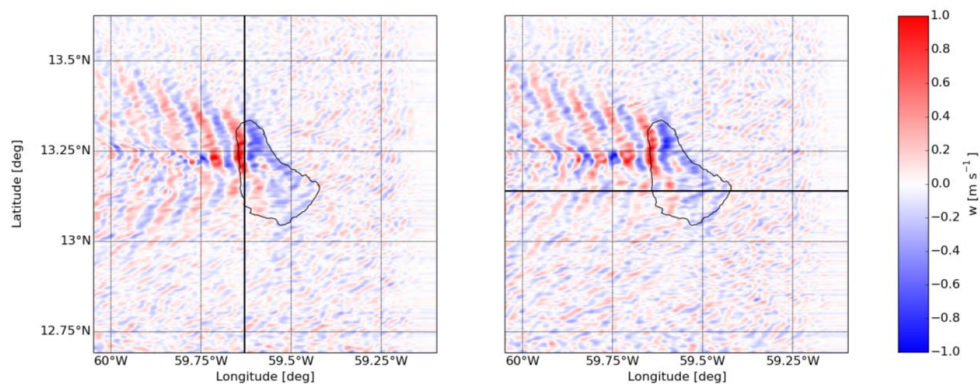
10



1

2 Figure 14. Retrieved backscatter coefficient (red) and vertical wind speed (blue) on the lee
3 side of Barbados during the flight of the 2nd leg at altitude of 1600 m. Due to the presence of
4 clouds, data between 21:56 and 21:57 LT is missing.

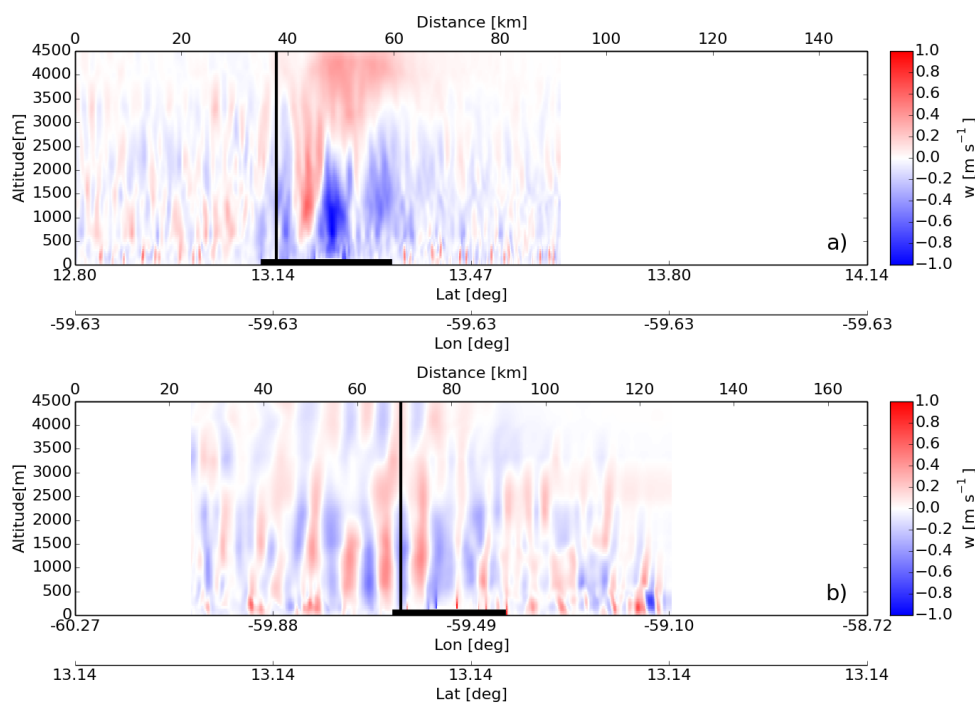
5



1

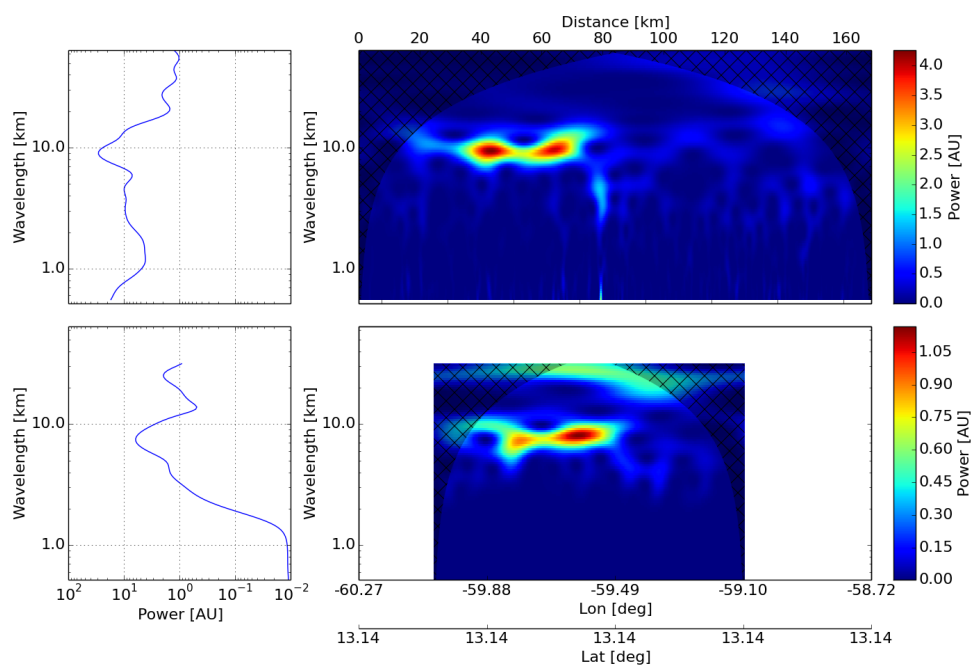
2 Figure 15. Vertical wind speed at 1975 m derived from the LES corresponding to 26 June at
3 20:00 LT (left panel) and 22:00 LT (right panel). The flight tracks corresponding to leg 1
4 (left) and 2 (right) are also indicated (solid, black).

5



1

2 Figure 16. Vertical wind speed from the LES for 26 June at 20:00 LT for leg 1 (upper panel)
3 and 22:00 LT for leg 2 (lower panel). The location of Barbados is indicated as a horizontal
4 black segment, while the intersection between legs 1 and 2 is indicated with a vertical line.



1
2 Figure 17. Wavelet analysis of the vertical wind corresponding to the 2nd leg for the flight on
3 26 June derived from the DWL measurements (Fig. 11, b) at 2000 m (upper panels) and
4 derived from the LES (Fig. 16, b) at 2000 m (lower panels). The hatched areas indicate the
5 cone of influence. The left panels show the average power for each wavelength.
6